Research on IPT Resonant Converters With High Misalignment Tolerance Using Multicoil Receiver Set

Guangjie Ke, Qianhong Chen, *Member, IEEE*, Wei Gao, Siu-Chung Wong, *Senior Member, IEEE*, Chi K. Tse, *Fellow, IEEE*, and Zhiliang Zhang, *Senior Member, IEEE*

***Abstract*—This article provides a comprehensive analysis of the contactless resonant converters using a multicoil receiver set for high misalignment tolerance, with emphasis on the cooperative mechanism of multiple coils and a quantitative analysis of the operating characteristics. The collaborative operation of multiple receiving coils with various compensation circuits and connection types is discussed. A series–parallel compensated converter using a DD2Q receiver set with parallel connection for the multiple rectified outputs is used to illustrate the analysis procedure. Two methods are presented here, namely numerical calculation for the normal case and analytical derivation under three typical misalignments. With the help of switching functions, the general output voltage gain can be derived, which provides direct insight into the cooperation of multiple coils and a practical approach for reducing the output fluctuation. Simulation and experimental verifications are included to confirm the analytical results.**

***Index Terms*—Inductive power transfer (IPT), misalignment tolerance, multicoil receiver, wireless power transfer.**

I. Introduction

THE inductive power transfer (IPT) technology, which transfers power through magnetic coupling, is safer, more flexible, and more convenient, compared to plug-in power transfer solutions. It is now used in a variety of applications, such as personal electronic devices, wearable/implantable electronics, electric vehicles, and so on [1]–[5]. However, the inevitable misalignment between the power transmitter and the receiver pads, which would cause coupling variations and hence impair the system's performance [6], [7], has become a major problem limiting IPT's applications [8], [9].

Much work has been done to improve the misalignment tolerance, mainly from the perspective of control strategies, compensation schemes and magnetic coupler designs, as shown in Fig. 1. Among the existing control strategies, the dynamic tuning control method proposed in [11]–[13] achieves large tolerance to misalignments. By adjusting an equivalent compensation capacitance or inductance, as illustrated in Fig. 1, the tuning condition for different misalignments can be either changed or satisfied, so as to improve the IPT system's performance [12]. However, this solution still suffers from increased complexity, extra cost, weight, and loss caused by the additional capacitor/inductor tuning circuit especially in high-power applications [13]. Compensation networks for achieving a larger tolerance to misalignments have also been investigated [15]–[21]. A general design method of primary compensation networks has been proposed to maintain a stable output characteristic [15]. It has been shown that some high-order compensations, such as S/SP [16], PS/S [17], SP/S [18], and LCC [21], could deliver almost constant power with small fluctuations under wide misalignments without additional control. Even with simple compensations like S/S, S/P, etc., a nonmonotonic output with better misalignment tolerance can be obtained through detuned parameter design [19], but with slightly lower efficiency due to the increased reactive power.

Being a significant part of an IPT system, the magnetic coupler is crucial for improving the misalignment tolerance. As summarized in Fig. 1, adopting a magnetic coupler with asymmetric structure by enlarging the physical size of either transmitter or the receiver coil is an effective method to improve the misalignment tolerance [22]. However, the mismatch between the transmitter and the receiver tends to reduce the coupling coefficient. Moreover, the typical ubiquitous powering pads [23], such as double-D pads (DDP) and circular pads, have the problem of null coupling which would greatly impair the power transfer capability. To alleviate the null coupling problem, structures with multidecoupled coils in either the transmitter or the receiver have been presented [24]–[30], as shown in Fig. 1. Multiple transmitting coils are utilized to establish the directional [24], [25] or omnidirectional magnetic field [26], [27] by individually controlling the current of each coil. However, the directional magnetic field control requires an additional location detection [24], and the omnidirectional field is energy inefficient for static charging due to the large amount of the uncoupled magnetic flux [27]. In contrast, magnetic coupler with multiple receiving windings is preferred [28]–[30]. Multiple receiving windings can compensate or switch automatically, so as to eliminate the null coupling problem and, hence, improve the misalignment tolerance effectively. In [29], a DDQ coil structure consisting of

Manuscript received March 17, 2019; revised June 27, 2019; accepted August 8, 2019. Date of publication August 19, 2019; date of current version January 10, 2020. This work was supported by the National Natural Science Foundation of China under Grant 51677086. Recommended for publication by Associate Editor S. C. Tan. *(Corresponding author: Qianhong Chen.)*

G. Ke, Q. Chen, W. Gao, and Z. Zhang are with the Aero-Power Sci-Tech Center, Nanjing University of Aeronautics and Astronautics, Nanjing 210016, China (e-mail: kegaungjie@nuaa.edu.cn; chenqh@nuaa.edu.cn; gaoweiee@nuaa.edu.cn; zlzhang@nuaa.edu.cn).

S.-C. Wong is with the Department of Electronic and Information Engineering, The Hong Kong Polytechnic University, Hong Kong, China (e-mail: enscwong@polyu.edu.hk).

C. K. Tse is with the Department of Electrical Engineering, City University of Hong Kong, Hong Kong, China (e-mail: cktse@ieee.org).

Color versions of one or more of the figures in this article are available online at http://ieeexplore.ieee.org

Digital Object Identifier 10.1109/TPEL.2019.2936325

See http://www.ieee.org/publications_standards/publications/rights/index.html for more information.

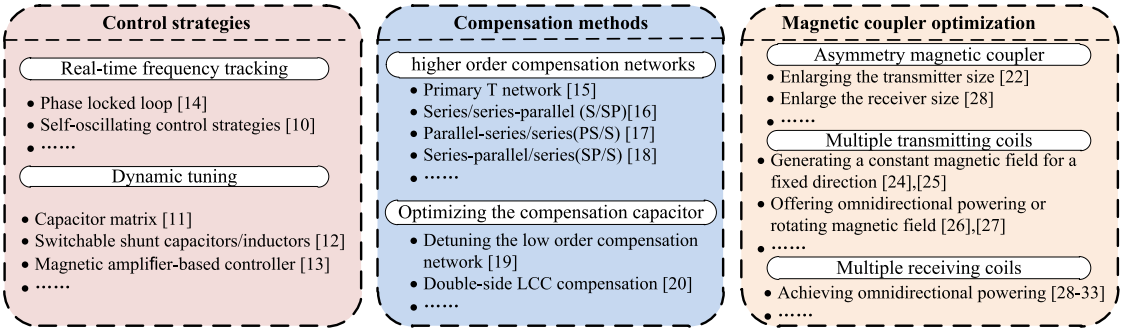

Fig. 1. Existing solutions to improve the misalignment tolerance.

a horizontal DD coil and a quadrature coil has been proposed to compensate misalignment in lateral direction. However, the DDQ structure has no improvement in angular displacement, which is unavoidable in practical application [31]. As a remedy, a DD2Q coil set consisting a classical DD winding and two additional quadrature windings (referred as 2Q) was proposed in [32]. Despite the positive experimental results on the misalignment tolerance, there is still a lack of quantitative analysis of the operation of multiple coils. In [33], two orthogonal receiving windings have been proposed to enhance the transfer efficiency under coil misalignment, and a detailed and accurate analysis has been performed using a canonical transformer model. However, the quantitative expressions given in [33] are too complicated to give any direct insight into the cooperative operation of the multiple receiving coils. Hence, a simple, easy-to-understand, and instructive description of the characteristic performance for an IPT converter adopting a multicoil receiver is necessary.

This article attempts to make an in-depth investigation into the contactless converters adopting multiple receiving coils. In Section II, a general analysis of the collaboration of the multiple receiving coils in an IPT converter is provided. A primary series/secondary parallel compensated contactless converter with multiple outputs connected in parallel (S/P-P in short) using a DD2Q receiver set is analyzed in detail. In Section III, a numerical method to obtain the output voltage gain and the input impendence of the S/P-P converter by determining the equivalent output conductances for different receiving coils is given. The output voltage gain for the selected converter under three typical misalignments is also derived. On this basis, the design procedure of the DD2Q receiver set for an S/P-P converter is given in Section IV. Experimental results are presented under various coupling conditions in Section V. Finally, Section VI concludes this article.

II. General Analysis for an IPT Converter With Multicoil Receiver

A. Circuit Implementations

The general circuit implementations of the IPT converters adopting a multicoil receiver, which comprises one transmitter and n ($\geq$2) receiver coils, are shown in Fig. 2, where L_p and L_{si} $(i = 1, 2, \ldots, n)$ are the respective inductances of the

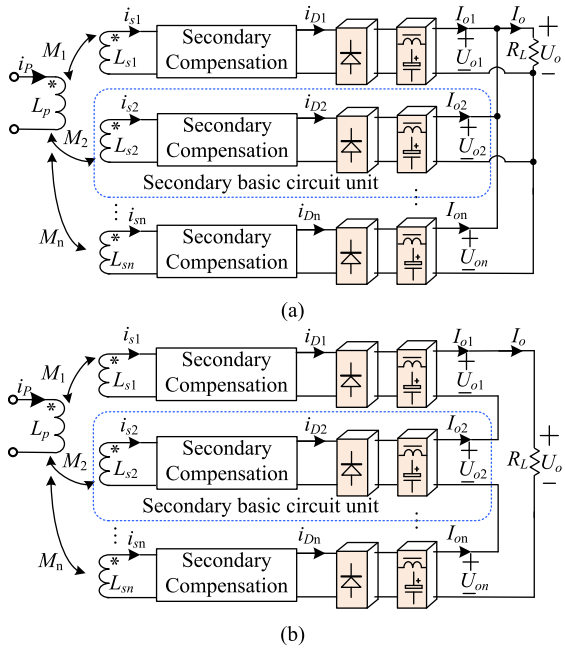

Fig. 2. Typical circuit implementations adopting a multicoil receiver. (a) Parallel connected. (b) Series connected.

coils, i_p and i_{si} are the respective winding currents, M_i is the mutual inductance between L_{si} and L_p. Each receiving coil and its corresponding compensation network, rectifier, and filter constitute the basic circuit unit of the secondary part. Here, i_{Di} is the ac input current of the ith rectifier, I_{oi}, and U_{oi} are the dc output current and output voltage of the ith basic circuit unit, and R_L is the load. Fig. 2 illustrates two typical connections for the rectified outputs: series or parallel connections. Since the analytical method and the analyzed results are similar, discussions of the other hybrid connections are omitted in this article.

The types of secondary compensation and output connection will affect the collaboration of the multiple coils. There are four basic configurations for the secondary circuits with multicoil receiver: series-compensation series-connection (S-S in short, with the first S denoting series compensation for the secondary and the latter S denoting series connection in the output, and

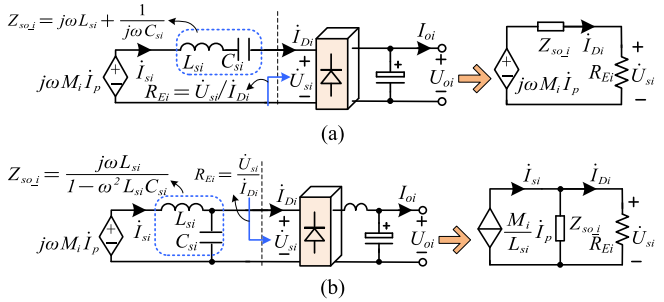

Fig. 3. Fundamental equivalent circuit of a secondary basic circuit unit ($i = 1, 2 \ldots n$). (a) Series compensation. (b) Parallel compensation.

likewise for other configurations), parallel-compensation series-connection (P-S), series-compensation parallel-connection (S-P), and parallel-compensation parallel-connection (P-P). Since a higher order secondary compensation can be reduced to a second order series or parallel compensation [17] in view of the equivalence of the output performance, only series or parallel compensation for the secondary circuit is considered here. Neglecting the cross coupling of the multiple receiving coils, the fundamental equivalent circuit of the secondary basic circuit unit can be obtained by employing fundamental harmonic approximation [16], as shown in Fig. 3. Here, all voltage and current variables are represented by the fundamental phasors, Z_{so_i} is the equivalent output impedance and the rectifier is represented by an equivalent resistance R_{Ei}, satisfying

$$\begin{cases} \sum_{i=1}^{n} R_{Ei} = R_E = \begin{cases} 8R_L/\pi^2 & \text{for S-S circuits} \\ \pi^2 R_L/8 & \text{for P-S circuits} \end{cases} \\ \sum_{i=1}^{n} \frac{1}{R_{Ei}} = \frac{1}{R_E} = \begin{cases} \pi^2/(8R_L) & \text{for S-P circuits} \\ 8/(\pi^2 R_L) & \text{for P-P circuits.} \end{cases} \end{cases} \tag{1}$$

B. Operating Modes

There are two operating states for each circuit unit: powering state or idling state. From Figs. 2 and 3, it is readily known that the $|\dot{I}_{Di}|$ of each circuit unit with series connection in powering state should be equal to a certain value I_B, i.e.,

$$\left|\dot{I}_{Di}\right| = I_B = \begin{cases} \left|\dfrac{\omega M_i \dot{I}_p}{Z_{so\_i} + R_{Ei}}\right| = \dfrac{\pi I_o}{2\sqrt{2}} & \text{for S-S circuits} \\ \left|\dfrac{M_i \dot{I}_p \left(R_{Ei} || Z_{so\_i}\right)}{L_{si} R_{Ei}}\right| = \dfrac{2\sqrt{2} I_o}{\pi} & \text{for P-S circuits.} \end{cases} \tag{2}$$

where $|\dot{I}_{Di}|$ stands for the RMS value of $\dot{I}_{Di}$, and likewise for other phasors. When $|\dot{I}_{Di}|$ is less than I_B, the two diodes of the same lag in the rectifier will conduct simultaneously, as shown in Fig. 4(a), clamping $\dot{U}_{si}$ zero, and thus, getting R_{Ei} to zero. Then, the circuit is in idling state.

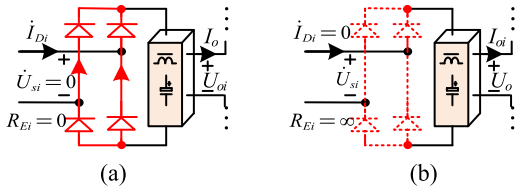

Fig. 4. Rectifiers in idling state. (a) Series connection. (b) Parallel connection.

Similarly, we can find that the $|\dot{U}_{si}|$ of a basic circuit employing parallel connection in powering state should equal to a certain value U_B, i.e.,

$$\left|\dot{U}_{si}\right| = U_B = \begin{cases} \left|\dfrac{M_i \dot{I}_p \left(R_{Ei} || Z_{so\_i}\right)}{L_{si}}\right| = \dfrac{\pi U_o}{2\sqrt{2}}, & \text{for P-P circuits} \\ \left|\dfrac{\omega M_i \dot{I}_p R_{Ei}}{R_{Ei} + Z_{so\_i}}\right| = \dfrac{2\sqrt{2} U_o}{\pi}, & \text{for S-P circuits.} \end{cases} \tag{3}$$

When $|\dot{U}_{si}| < U_B$, the diodes in the rectifier will be blocked, indicating the circuit being in idling state, resulting in a zero $|\dot{I}_{Di}|$, and an infinite R_{Ei}, as shown in Fig. 4(b).

Considering the collaboration of secondary coils, multiple operating modes exist for a multicoil receiver. The maximum number of operating modes can be determined by ΣC_n^i. For example, when *n* equals 3, there are three operating modes for only one secondary coil in the powering state, the three operating modes with two secondary coils powering the load and one operating mode for three secondary coils in powering state at the same time.

C. Collaboration of the Multiple Coils

Fig. 3 indicates that the series or parallel compensated basic circuit can be equivalent to a voltage source or a current source with an internal impedance, respectively. So, the collaboration of multiple coils is just the cooperation of multiple voltage sources or current sources, each having its internal impedance. Two cases of tuned and detuned operating frequency will be considered in the following sections.

1) $\omega = \omega_s = 1/\sqrt{L_{si} C_{si}}$*:* Secondary circuits operating at ω_s means $Z_{so\_i} = 0$ for series compensation or $Z_{so\_i} = \infty$ for parallel compensation. As it can be seen in Fig. 3, a basic circuit adopting series or parallel compensation is equivalent to a voltage source or current source. Thus, the secondary S-S/S-P and P-S/P-P circuits adopting *n* coils at ω_s behave as *n* voltage sources connected in series/in parallel through rectifiers, the *n* current sources connected in series/in parallel through rectifiers, respectively. Since multiple voltage sources/current sources are easy to be connected in series/in parallel, the multiple coils of the secondary S-S or P-P circuits could power the load simultaneously.

Substituting $Z_{so\_i}=0$ into (2) and $Z_{so\_i}=\infty$ into (3) yields the conditions of powering states at ω_s, i.e.,

$$\left|\dot{I}_{Di}\right|=\begin{cases}\left|\omega_s M_i\dot{I}_p\right|/R_{Ei}=\frac{\pi I_o}{2\sqrt{2}} & \text{for S-S circuits}\\ \left|M_i\dot{I}_p\right|/L_{si}=2\sqrt{2}I_o/\pi & \text{for P-S circuits}\end{cases} \tag{4}$$

$$\left|\dot{U}_{si}\right|=\begin{cases}\left|M_i\dot{I}_p R_{Ei}\right|/L_{si}=\pi U_o/\left(2\sqrt{2}\right) & \text{for P-P circuits}\\ \left|\omega_s M_i\dot{I}_p\right|=2\sqrt{2}U_o/\pi & \text{for S-P circuits.}\end{cases} \tag{5}$$

It can be seen from (4) and (5) that the higher the value of M_i, the larger the value of R_{Ei} and the output power for an S-S circuit, and the lower the value of R_{Ei} and the larger the output power for a P-P circuit. This is the inherent regulating rule for S-S and P-P circuits adopting a multicoil receiver. Most of the receiver coils of the S-S or P-P circuits operating at ω_s will power the load simultaneously. Since the mutual inductances of the multiple coils are different, (4) or (5) applies to only one coil with the maximum mutual inductance in the S-P or P-S circuit. In other words, only one coil will power the load for the S-P or P-S circuit at ω_s. Neglecting the cross coupling between the multiple receiving coils, the dc output voltage U_o can be easily obtained by the superposition of U_{oi} for S-S or P-S circuit, and the dc output current I_o can be easily obtained by the superposition of I_{oi}, yielding U_o. Therefore, we have

$$U_o=\begin{cases}\pi/\left(2\sqrt{2}\right)\sum_{i=1,R_{Ei}\neq 0}^{n}\left|\omega_s M_i\dot{I}_P\right| & \text{for S-S circuits}\\ \pi R_L/\left(2\sqrt{2}\right)\max\left(\left|M_i/L_{si}\right|\right)\left|\dot{I}_P\right| & \text{for P-S circuits}\\ \pi R_L/\left(2\sqrt{2}\right)\sum_{i=1,R_{Ei}\neq\infty}^{n}\left(\left|M_i/L_{si}\right|\right)\left|\dot{I}_P\right| & \text{for P-P circuits}\\ \pi/\left(2\sqrt{2}\right)\max\left(\left|\omega_s M_i\right|\right)\left|\dot{I}_P\right| & \text{for S-P circuits.}\end{cases} \tag{6}$$

From (6), we clearly see that the combined effect of the multiple coils, each having a different null coupling position, alleviates the null power problem, and hence permits the converter to achieve improved performance against coupling variations, similar to the use of interleaving for combating fluctuations and reducing ripples. Besides, (6) indicates that the S-S and S-P circuits are suitable for the constant voltage output applications, whereas the P-S and P-P circuits are suitable for constant current output applications.

Considering $U_o=R_L I_o$, combining (4) and (5) with (6) gives the expression for R_{Ei} for S-S and S-P circuits, i.e.,

$$R_{Ei}=\begin{cases}\left|M_i\right|R_E/\sum_{j=1}^{n}\left|M_j\right| & \text{for S-S circuits}\\ \frac{R_E L_{si}}{\left|M_i\right|}\left(\sum_{j=1}^{n}\frac{\left|M_j\right|}{L_{sj}}\right) & \text{for P-P circuits.}\end{cases} \tag{7}$$

2) $\omega\neq\omega_s$: When $\omega\neq\omega_s$, we have $Z_{so\_i}\neq 0$ for series compensation and $Z_{so\_i}\neq\infty$ for parallel compensation. Since $Z_{so\_i}\neq 0$ or $Z_{so\_i}\neq\infty$, $\dot{U}_{si}$ or $\dot{I}_{Di}$ can be regulated by adjusting R_{Ei} to satisfy the conditions of powering states given in (2) and (3). Thus, the multiple receiving coils of four typical circuits under detuned condition could power the load at the same time, even for S-P and P-S circuits. This can be easily understood according to the collaboration of the multiple voltage/current sources with internal impedances connected through the rectifiers. In a similar manner, the output voltage for all four types of secondary circuits can be obtained. The collaboration of multiple coils with different mutual inductances helps to reduce the output fluctuations under misalignments.

$$U_o=\begin{cases}\frac{\pi}{2\sqrt{2}}\sum_{i=1,R_{Ei}\neq 0}^{n}\left|\frac{\omega M_i\dot{I}_p R_{Ei}}{Z_{so\_i}+R_{Ei}}\right| & \text{for S-S circuits}\\ \frac{2\sqrt{2}}{\pi}\sum_{i=1,R_{Ei}\neq 0}^{n}\left|\frac{M_i\dot{I}_p\left(R_{Ei}||Z_{so\_i}\right)}{L_{si}}\right| & \text{for P-S circuits}\\ \frac{\pi R_L}{2\sqrt{2}}\sum_{i=1,R_{Ei}\neq\infty}^{n}\left|\frac{M_i\dot{I}_p\left(R_{Ei}||Z_{so\_i}\right)}{L_{si}R_{Ei}}\right| & \text{for P-P circuits}\\ \frac{2\sqrt{2}R_L}{\pi}\sum_{i=1,R_{Ei}\neq\infty}^{n}\left|\frac{\omega M_i\dot{I}_p}{R_{Ei}+Z_{so\_i}}\right| & \text{for S-P circuits.}\end{cases} \tag{8}$$

Note that U_o might also follow the maximum rule. For instance, for an S-P circuit, the *i*th circuit unit will be in an idling state when

$$\left|j\omega M_i\dot{I}_p\right|<\left|j\omega M_j\dot{I}_p\right|\left(\frac{Z_{so\_j}}{R_E}+1\right)^{-1},\ M_j=\max\left\{M_i\right\} \tag{9}$$

where $i=1,\ 2,\ldots,$ or *n*. If all the other coils $(i\neq j)$ are in idling states, the output voltage is

$$U_o=\max\left\{\frac{2\sqrt{2}}{\pi}\left|j\omega M_i\dot{I}_p\right|\left(\frac{Z_{so\_i}}{R_E}+1\right)^{-1}\right\}. \tag{10}$$

If some of the basic circuit units are fully tuned but others are not, the tuned basic circuit units will operate according to the collaboration rules at ω_s and then collaborate with other parts according to the detuned rules.

D. Simulation Verification

Figs. 5 and 6 show the simulated waveforms of $u_{s\mathrm{i}}$ and $i_{D\mathrm{i}}$ along with their RMS values for the IPT converters with a two-coil receiver, operating at the tuned frequency f_s 120 kHz $(\omega_s=2\pi f_s)$ and detuned frequency 140 kHz, adopting S-S, S-P, P-S, and P-P configurations, respectively. The four simulation circuits share the same ω_s, dc input voltage, and *LCL* network yielding the same primary $|\dot{I}_p|$. The simulation circuits, which can be easily obtained according to Figs. 2 and 3, are omitted for brevity. Table I lists the detailed simulation parameters. It should be noted that the distinct difference between M_1 (7.14 μH) and M_2 (5.89 μH) is to emulate the effect of the misalignment. The load resistance is set as 5 Ω for the S-S and S-P circuits and as 50 Ω for the P-S and P-P circuits.

When $f=120$ kHz, it can be readily seen from Fig. 5 that $|\dot{I}_{D1}|=|\dot{I}_{D2}|$ for the S-S circuit, $|\dot{I}_{D2}|=0$ for the S-P circuit, $|\dot{U}_{s2}|\approx 0$ for the P-S circuit, and $|\dot{U}_{s1}|=|\dot{U}_{s2}|$ for the P-P circuit. Thus, for S-P and P-S circuits, only the coil L_{s1} with

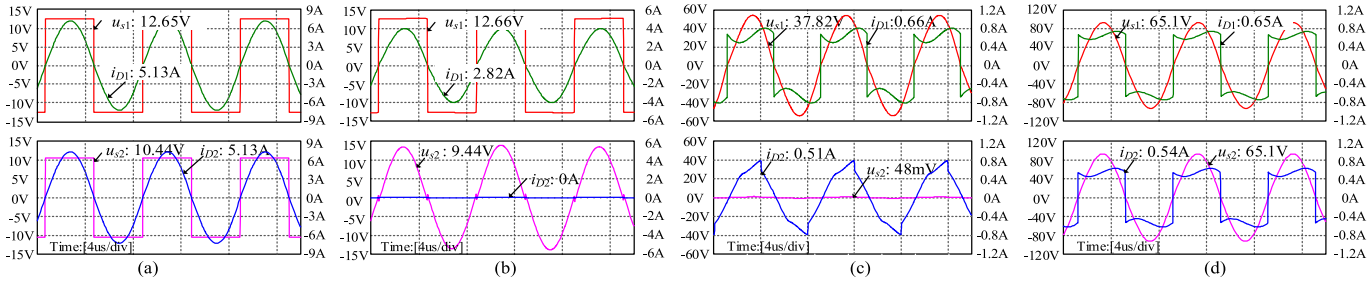

Fig. 5. Simulated waveforms of the four secondary basic configurations at 120 kHz ($\omega = \omega_s$). (a) S-S. (b) S-P. (c) P-S. (d) P-P.

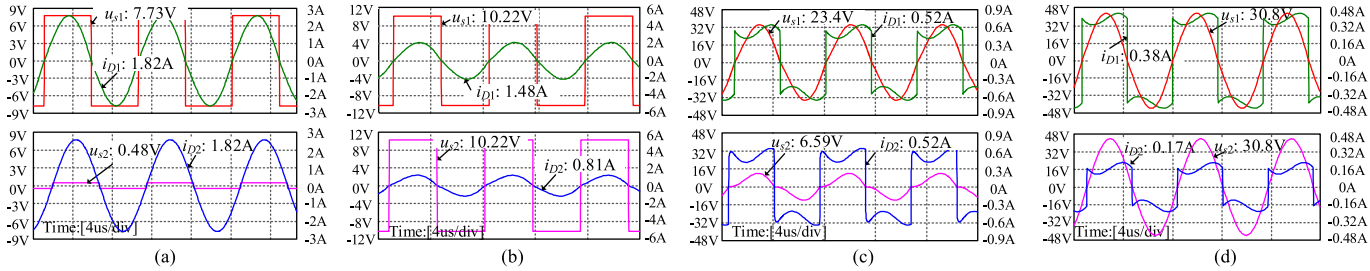

Fig. 6. Simulated waveforms of the four secondary basic configurations at 140 kHz ($\omega \neq \omega_s$). (a) S-S. (b) S-P. (c) P-S. (d) P-P.

TABLE I
PARAMETERS OF THE SIMULATION CIRCUITS

$\lvert\dot{I}_p\rvert$/A	f/kHz	L_p/μH	L_{s1}/μH	L_{s2}/μH	C_{s1}/nF	C_{s2}/nF	M_1/μH	M_2/μH	R_L/Ω
2.12	120	25.33	26.01	25.89	67.63	67.94	7.14	5.89	5/50

TABLE II
CALCULATED AND SIMULATED U_o AND I_o FOR FOUR TYPES OF SECONDARY CIRCUITS AT 120 kHz ($\omega = \omega_s$)

Circuit		S-S	S-P	P-S	P-P
Sim.	U_o/V	23.084	12.66	32.434	58.48
	I_o/ A	4.617	2.53	0.648	1.17
Cal.	U_o/V	23.145	12.679	32.33	59.13
	I_o/ A	4.629	2.536	0.647	1.18

a larger mutual inductance powers the load, whereas for the S-S and P-P configurations, L_{s1} and L_{s2} power the load simultaneously, and L_{s1} provides a larger portion of the power, confirming the previous analysis. When $f = 140$ kHz, as shown in Fig. 6, we have $|\dot{I}_{D1}| = |\dot{I}_{D2}|$ for the S-S circuit and $|\dot{U}_{s1}| = |\dot{U}_{s2}|$ for the P-P circuit, whereas $|\dot{I}_{D1}| = |\dot{I}_{D2}|$ for the P-S circuit and $|\dot{U}_{s1}| = |\dot{U}_{s2}|$ for the S-P circuit, verifying that the multiple receiving coils under detuned condition can power the load at the same time. Tables II and III give the calculated and the simulated values of U_o and I_o, at 120 kHz and 140 kHz, respectively. It can be found that under both tuned and detuned conditions, the calculated results are consistent with the simulated results.

III. ANALYSIS OF AN S/P-P CONVERTER USING DD2Q RECEIVER SET

In Section II, the collaboration of multiple receiving coils for different circuit configurations has been analyzed. The characteristics are expressed in terms of $\dot{I}_p$, making the analysis more convenient when the primary current is constant [28], [31]. But for most IPT converters, the primary coil current is dependent on M_i and R_{Ei}, which will increase the complexity of the analysis greatly. In this section, an S/P-P converter using a DD2Q receiver set is adopted as an example to perform the investigation.

TABLE III
CALCULATED AND SIMULATED U_o AND I_o FOR FOUR TYPES OF SECONDARY CIRCUITS AT 140 kHz ($\omega \neq \omega_s$)

Circuit		S-S	S-P	P-S	P-P
Sim.	U_o/V	8.18	10.23	26.24	27.653
	I_o/ A	1.635	2.046	0.524	0.553
Cal.	U_o/V	8.188	10.75	26.023	26.5
	I_o/ A	1.638	2.15	0.52	0.53

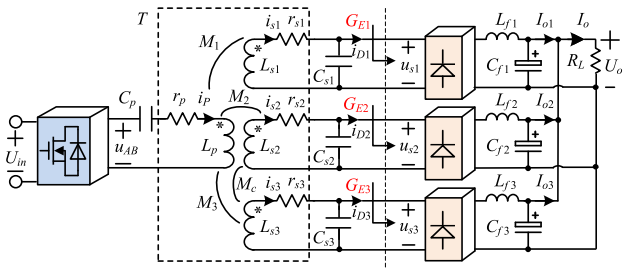

Fig. 7. S/P-P converter with DD-DD2Q structure.

A. Circuit Description

Fig. 7 illustrates the schematic of an S/P-P converter that employs S/P compensation and parallel connection for three rectified outputs. The contactless transformer T adopts a DD transmitter (pri-DD winding) and a DD2Q three-coil receiver set that comprises a classical DD winding (sec-DD winding) and

TABLE IV
COMPENSATION CAPACITANCES OF S/P-P CONVERTER

C_p	C_{s1}	C_{s2}	C_{s3}
$\frac{1}{\omega_s^2(L_p - M_{1\_0}^2/L_{s1})}$	$\frac{1}{\omega_s^2 L_{s1}}$	$\frac{1}{\omega_s^2(L_{s2}+M_c)}$	$\frac{1}{\omega_s^2(L_{s3}+M_c)}$

TABLE V
OPERATING MODES AND EQUIVALENT CONDUCTANCES

m	Powering Coil(s)	Modes Definition		G_{Ei}
1	L_{sj} $M_j = \max(M_i)$	DD	1:$j=1$	$G_{Ek}=0$ $G_{Ej}=G_E$
		Q1	2:$j=2$	
		Q2	3:$j=3$	
2	L_{sj} $M_j \neq \min(M_i)$	DD, Q1	4:$k=3$	$G_{Ek}=0$ $\sum G_{Ej}=G_E$
		DD, Q2	5:$k=2$	
		Q1, Q2	6:$k=1$	
3	L_{s1}, L_{s2}, L_{s3}	DD, Q1, Q2	7:$j=1, 2, 3$	$\sum_{j=1}^{3} G_{Ej}=G_E$

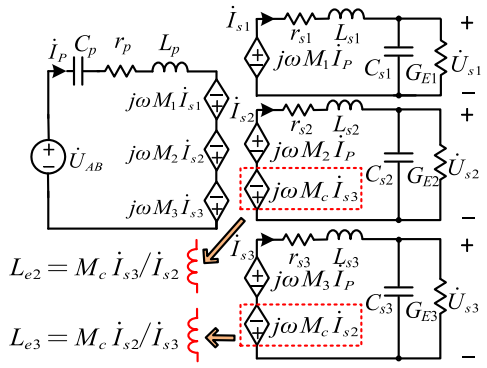

Fig. 8. Equivalent circuit of S/P-P converter.

two additional quadrature windings Q1 and Q2. Thus, n is 3 and there are seven operating modes, as listed in Table V. To comply with the parameter definition in Section II, we use subscripts "p," "$_1$," "$_2$," and "$_3$" to denote the windings of pri-DD, sec-DD, Q1, and Q2, respectively. Also, L_p, L_{s1}, L_{s2} and L_{s3}, r_p, r_{s1}, r_{s2}, and r_{s3} denote the inductances and resistances of the windings of pri-DD, sec-DD, and Q1 and Q2, respectively; M_1, M_2, and M_3 are the respective mutual inductances between L_p/L_{s1}, L_p/L_{s2}, L_p/L_{s3}, and likewise for other variables. Since Q1 and Q2 are magnetically decoupled from sec-DD winding [32], only the cross coupling M_c between Q1 and Q2 is considered here. As shown in Fig. 7, powered by the dc voltage source U_{in}, the inverter produces an ac voltage u_{AB} to drive the resonant tank to achieve the power transfer.

B. Numerical Calculation Method

Fig. 8 illustrates the fundamental equivalent circuits for the primary and the secondary. Substituting $n = 3$ into (1) and introducing the equivalent load conductances G_{Ei} for the basic circuits, we have

$$\sum_{i=1}^{3} G_{Ei} = G_E = 8/\left(\pi^2 R_L\right). \tag{11}$$

According to Fig. 8, the following equation can be obtained:

$$\begin{bmatrix} \dot{U}_{AB} \\ 0 \\ 0 \\ 0 \end{bmatrix} = \begin{bmatrix} Z_p & -j\omega M_1 & -j\omega M_2 & -j\omega M_3 \\ -j\omega M_1 & Z_{s1} & 0 & 0 \\ -j\omega M_2 & 0 & Z_{s2} & j\omega M_c \\ -j\omega M_3 & 0 & j\omega M_c & Z_{s3} \end{bmatrix} \begin{bmatrix} \dot{I}_p \\ \dot{I}_{s1} \\ \dot{I}_{s2} \\ \dot{I}_{s3} \end{bmatrix} \tag{12}$$

where $Z_{si} = j\omega L_{si} + r_{si} + \frac{1}{j\omega C_{si}+G_{Ei}}, i=1,2,3, Z_p = j\omega L_p + r_p + \frac{1}{j\omega C_p}$.

The two bottom equations of (12) can also be expressed as

$$\begin{aligned} j\omega M_2\dot{I}_p &= \left(Z_{s2} + j\omega M_c\dot{I}_{s3}/\dot{I}_{s2}\right)\dot{I}_{s2}, j\omega M_3\dot{I}_p \\ &= \left(Z_{s3} + j\omega M_c\dot{I}_{s2}/\dot{I}_{s3}\right)\dot{I}_{s3}. \end{aligned} \tag{13}$$

It is found that the cross coupling can be equivalent to virtual inductances L_{e2} and L_{e3} with $L_{e2} = M_c\dot{I}_{s3}/\dot{I}_{s2}$ and $L_{e3} = M_c\dot{I}_{s2}/\dot{I}_{s3}$, as shown in Fig. 8. In particular, when $\dot{I}_{s2} = \dot{I}_{s3}$, the values of L_{e2} and L_{e3} are constant and are equal to M_c. Similar to that of the conventional S/P compensated converter [34], the compensated capacitors of S/P-P converter can be designed according to Table IV, where C_{si} is resonant with the respective equivalent inductance at ω_0 and C_p is designed to achieve zero input phase angle at M_{1_0}. M_{1_0} represents the mutual inductance between L_p/L_{s1} at the designed point.

Solving (12) gives

$$\begin{bmatrix} \dot{I}_{s1} \\ \dot{I}_{s2} \\ \dot{I}_{s3} \end{bmatrix} = \begin{bmatrix} j\omega M_1/Z_{s1} \\ \left(j\omega M_2 Z_{s3} + \omega^2 M_c M_3\right)/\left(\omega^2 M_c^2 + Z_{s2}Z_{s3}\right) \\ \left(j\omega M_3 Z_{s2} + \omega^2 M_c M_2\right)/\left(\omega^2 M_c^2 + Z_{s2}Z_{s3}\right) \end{bmatrix} \dot{I}_p. \tag{14}$$

The input impedance Z_{in} and the voltage gains of G_{v1}, G_{v2}, and G_{v3} can then be derived as

$$\begin{aligned} Z_{\text{in}} = \frac{\dot{U}_{AB}}{\dot{I}_p} &= Z_p + \frac{(\omega M_1)^2}{Z_{s1}} \\ &\quad - \frac{-\omega^2\left(M_2^2 Z_{s3} + M_3^2 Z_{s2}\right) + 2j\omega^3 M_2 M_c M_3}{\omega^2 M_c^2 + Z_{s2}Z_{s3}} \end{aligned} \tag{15}$$

$$\begin{cases} G_{v1} = \left|\dfrac{\dot{U}_{s1}}{\dot{U}_{AB}}\right| = \left|\dfrac{j\omega M_1}{Z_{s1}Z_{in}\left(j\omega C_{s1} + G_{E1}\right)}\right| \\ G_{v2} = \left|\dfrac{\dot{U}_{s2}}{\dot{U}_{AB}}\right| = \left|\dfrac{j\omega M_2 Z_{s3} + \omega^2 M_c M_3}{\left(\omega^2 M_c^2 + Z_{s2}Z_{s3}\right) Z_{\text{in}}\left(j\omega C_{s2} + G_{E2}\right)}\right| \\ G_{v3} = \left|\dfrac{\dot{U}_{s3}}{\dot{U}_{AB}}\right| = \left|\dfrac{j\omega M_3 Z_{s2} + \omega^2 M_c M_2}{\left(\omega^2 M_c^2 + Z_{s2}Z_{s3}\right) Z_{\text{in}}\left(j\omega C_{s3} + G_{E3}\right)}\right|. \end{cases} \tag{16}$$

For a full-bridge inverter and rectifier, we have $|\dot{U}_{AB}| = 2\sqrt{2}U_{\text{in}}/\pi$ and $|\dot{U}_{si}| = \pi U_o/(2\sqrt{2})$. Thus, if coil L_{si} is in powering mode, the dc voltage gain should satisfy

$$G_v = U_o/U_{\text{in}} = 8/\pi^2 G_{vi}. \tag{17}$$

It is obvious that to calculate G_v, we should first determine the operating modes of the multiple coils. Considering the interactions among G_{Ei}, G_{vi}, and the operating modes, a numerical

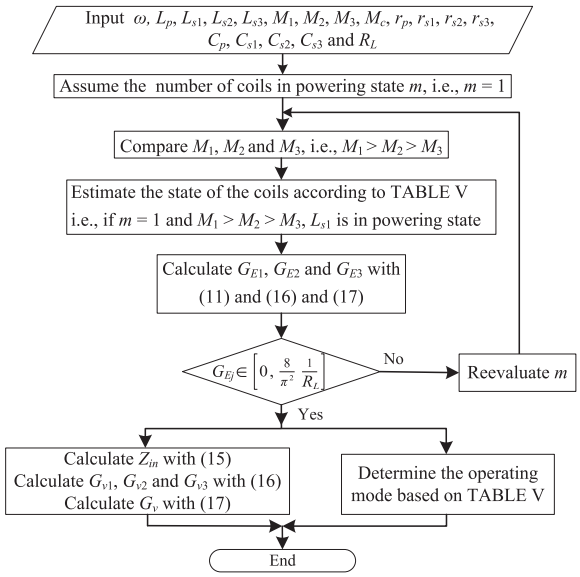

Fig. 9. Flowchart for calculation of parameters.

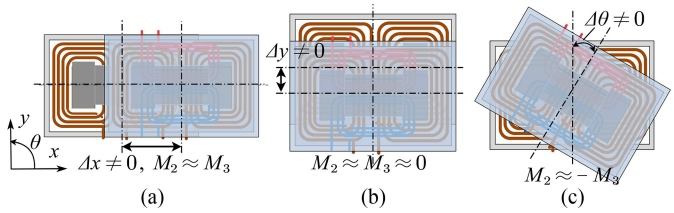

Fig. 10. Three typical misalignments in (a) lateral, (b) longitudinal, and (c) angular directions.

TABLE VI
SWITCHING FUNCTIONS IN DIFFERENT MODES AT ω_s

Mode 1			Mode 6			Mode 7		
S_1	S_2	S_3	S_1	S_2	S_3	S_1	S_2	S_3
1	0	0	0	1	1	1	1	1

solution is provided for the analysis, as illustrated in Fig. 9. First, we assume that the number of coils in the powering mode is *m* after obtaining the circuit parameters. Then, based on the assumed *m* and the known mutual inductances, the operating modes of the coils can be estimated according to Table V, where subscript "j" represents the coil in powering state, subscript "k" represents the coil in idling state. As tabulated in Table V, if $m = 1$, the coil having the maximum mutual inductance will be in powering state; if $m = 2$, the coil having the minimum mutual inductance will be in idling state. Next, the three equivalent conductances will be solved from (11), (16), and (17). If there is no real solution for G_{Ei} or G_{Ei} is outside the range of $[0,\ 8/(\pi^2 R_L)]$, the assumption of *m* is invalid and another calculation is needed. After getting the G_{Ei}, Z_{in} and G_v can then be finally calculated according to (15)–(17). Obviously, the calculation method used for generating results in Fig. 9 requires knowledge of the parasitic resistances, the self-inductances and the three mutual inductances, etc., which have to be measured or found from three-dimensional (3-D) finite-element simulation.

C. Analytical Derivation of S/P-P Converter Under Three Typical Misalignments

As discussed previously, G_{Ei}, G_{vi}, and the operating modes are interdependent, making it difficult to obtain analytical expressions of the characteristics of S/P-P converter in all seven operating modes. To simplify the analysis without loss of generality, this article combines the three typical misalignments, as illustrated in Fig. 10, to give further analytical derivation. In Fig. 10, Δx, Δy, and $\Delta\theta$ represent the misaligned distance/angular in lateral, longitudinal, and angular directions, respectively.

Since the two quadrature windings are symmetrically wound, there are $L_{s2} = L_{s3}, C_{s2} = C_{s3}, r_{s2} = r_{s3}$ [32]. Besides, under the three typical misalignments, we always have $|M_2| \approx |M_3|$ due to the symmetrical positions for Q1 and Q2 related to the primary. So it can be readily derived that $|\dot{I}_{s2}| = |\dot{I}_{s3}|$. Then, according to Fig. 8, we have $L_{e2} = L_{e3} \approx |M_C|$, which is not affected by misalignments. Under such cases, Q1 and Q2 always operate in the same state. Thus, only three operating modes: Mode 1, Mode 6, and Mode 7 exist under the three typical misalignments. For brevity, r_p, r_{s1}, r_{s2}, and r_{s3} are taken as zero in the following analysis, since they are relatively small and have limited influence on the characteristics.

Combining the capacitance formulas in Table IV with (11) and (17), the equivalent conductances at ω_s for Mode 1, Mode 6, and Mode 7 can be derived as

$$\begin{cases} G_{E1} = \\ \quad S_1 G_E \Big/ \left[S_2 \left|\dfrac{M_2}{M_1}\right| \dfrac{L_{s1}}{L_{s2}+L_{e2}} + S_3 \left|\dfrac{M_3}{M_1}\right| \dfrac{L_{s1}}{L_{s3}+L_{e3}} + 1 \right] \\ G_{E2} = \\ \quad S_2 G_E \Big/ \left[S_1 \left|\dfrac{M_1}{M_2}\right| \dfrac{L_{s2}+L_{e2}}{L_{s1}} + 1 + S_3 \left|\dfrac{M_3}{M_2}\right| \dfrac{L_{s2}+L_{e2}}{L_{s3}+L_{e3}} \right] \\ G_{E3} = \\ \quad S_3 G_E \Big/ \left[S_1 \left|\dfrac{M_1}{M_3}\right| \dfrac{L_{s3}+L_{e3}}{L_{s1}} + S_2 \left|\dfrac{M_2}{M_3}\right| \dfrac{L_{s3}+L_{e3}}{L_{s2}+L_{e2}} + 1 \right] \end{cases} \tag{18}$$

where the switching functions of S_1, S_2, and S_3 are introduced to define the operating states of L_{s1}, L_{s2}, and L_{s3}, as listed in Table VI. For instance, $S_1 = 0$ or 1 means L_{s1} being in idling state or powering state, respectively. As analyzed in Section II, for S/P-P converters, the smaller the M_i, the lower the output power and smaller the value of G_{Ei}. When G_{Ei} approaches zero, the operating mode will change.

Letting G_{E2} and G_{E3} of Mode 7 equal to 0 and $|\dot{U}_{s1}| = \sqrt{2}|\dot{U}_{s2}| = \sqrt{2}|\dot{U}_{s3}|$, the boundary between Mode 7 and Mode 1 can be obtained, as derived in the Appendix. Combining the

corresponding formulas in Table IV with (16) and (18), gives

$$\frac{k_1}{k_2}=\frac{\sqrt{(A_1-1)^2+(G_E\omega L_{si})^2}}{A_2\left(k_{e2}+1\right)-1}\sqrt{\frac{2L_{s2}}{L_{s1}}}\approx\sqrt{1+\left(\frac{Q_{s1}}{\omega^2/\omega_s^2-1}\right)^2}\sqrt{\frac{2L_{s2}}{L_{s1}}}. \tag{19}$$

Letting $G_{E1}=0$ and $\sqrt{2}|\dot{U}_{s1}|=|\dot{U}_{s2}|=|\dot{U}_{s3}|$, the boundary between Mode 7 and Mode 6 can also be derived as

$$\frac{k_2}{k_1}=\frac{\sqrt{4[A_2\left(k_{e2}+1\right)-1]^2+[G_E\omega L_{s2}\left(k_{e2}+1\right)]^2}}{\sqrt{2}\left(A_1-1\right)}\sqrt{\frac{L_{s1}}{L_{s2}}}\approx\sqrt{1+\left[\frac{Q_{s2}\left(k_{e2}+1\right)}{2\left(\omega^2/\omega_s^2-1\right)}\right]^2}\sqrt{\frac{L_{s1}}{2L_{s2}}} \tag{20}$$

where $k_{e2}=L_{e2}/\sqrt{L_{s2}L_{s3}}$, $A_i=\omega^2L_{si}C_{si}$, and $Q_{si}=\omega L_{si}G_E$, with $i=1, 2, 3$.

Substituting the capacitances given in Table IV and the equivalent conductances in (18) into (16), the output to input voltage gain and the input impedance for Mode 1, Mode 6, and Mode 7 can be derived, as given in the Appendix. With the help of S_1, S_2, and S_3, the general expressions for G_v and $Z_{\rm in}$ at ω_s under the three typical misalignments can then be found as

$$G_v|_{\omega=\omega_s}=\frac{S_1\frac{|M_1|}{L_{s1}}+\frac{S_2|M_2|}{L_{s2}+L_{e2}}+\frac{S_3|M_3|}{L_{s3}+L_{e3}}}{\left|Z_{\rm in}|_{\omega=\omega_s}G_E\right|}=\frac{S_1\left|k_1n_1\right|+S_2\left|\frac{k_2n_2}{1+k_{e2}}\right|+S_3\left|\frac{k_3n_3}{1+k_{e3}}\right|}{\left|Z_{\rm in}|_{\omega=\omega_s}G_E\right|} \tag{21}$$

$$\begin{aligned}Z_{\rm in}|_{\omega=\omega_s}=&\,j\omega_sL_p\left\{k_{1\_0}^2-\left(S_1k_1^2+S_2k_2^2/(1+k_{e2})\right.\right.\\&\left.\left.+S_3k_3^2/(1+k_{e3})\right)\right\}\\&+R_E\left[S_1\left|M_1\right|/L_{s1}+S_2\left|M_2\right|/(L_{s2}+L_{e2})\right.\\&\left.+S_3\left|M_3\right|/(L_{s3}+L_{e3})\right]\end{aligned} \tag{22}$$

where k_i is the coupling coefficient between L_p and L_{si}, k_{1_0} is the coupling coefficient between L_p/L_{s1} under the designed condition, and $n_i=\sqrt{L_p/L_{si}}$ is approximately the turns ratio of L_p and L_{si}. When fully aligned, $S_2=S_3=0$, the S/P-P converter with DD-DD2Q structure has the same characteristics as the conventional S/P compensated converter with the DD-DD structure.

Substituting (22) into (21), we have

$$\begin{aligned}G_v\,|_{\omega=\omega_s}&=1\Big/\left[jG_E\Delta+S_1\left|k_1n_1\right|+S_2\left|\frac{k_2n_2}{1+k_{e2}}\right|+S_3\left|\frac{k_3n_3}{1+k_{e3}}\right|\right]\\&=1\big/[S_1\left|k_1n_1\right|+S_2\left|k_2\right|n_2/(1+k_{e2})\\&\quad+S_3\left|k_3\right|n_3/\left(1+k_{e3}\right)]|_{\,\Delta=0}\end{aligned} \tag{23}$$

where

$$\begin{cases}\Delta=K\omega_sL_p\Big/\left[S_1\left|k_1n_1\right|+S_2\left|\frac{k_2n_2}{1+k_{e2}}\right|+S_3\left|\frac{k_3n_3}{1+k_{e3}}\right|\right]\\K=k_{1\_0}^2-\left[S_1k_1^2+S_2k_2^2/(1+k_{e2})+S_3k_3^2/(1+k_{e3})\right].\end{cases} \tag{24}$$

The detailed derivation of (19) to (24) will be given in the Appendix.

Equation (23) indicates that the output gain of S/P-P converter at ω_s is load-independent when $K=\Delta=0$. It can also be found that the opposite trends of k_2 (k_3) and k_1 during misalignments help to reduce the output fluctuation. Obviously, the parameter design of the DD2Q receiver set is important for the performance of the S/P-P converter.

IV. Design of the DD2Q Receiver Set for an S/P-P Converter

In this section, we demonstrate how a DD2Q receiver can be designed for reducing the output fluctuation. As discussed in Section II, the multiple coils would normally power the load simultaneously for P-P configuration. Substituting $S_1=S_2=S_3=1$ into (23) gives

$$G_v\approx1/[|k_1n_1|+|k_2n_2/(1+k_{e2})|+|k_3n_3/(1+k_{e3})|]. \tag{25}$$

Writing the denominator of (25) as H, we have

$$\begin{cases}H=H_{DD}+H_{Q\Sigma}\\H_{DD}=|k_1n_1|,\ H_{Q\Sigma}=\left|\frac{k_2n_2}{1+k_{e2}}\right|+\left|\frac{k_3n_3}{1+k_{e3}}\right|\\\qquad\qquad\approx2\left|\frac{k_2n_2}{1+k_{e2}}\right|.\end{cases} \tag{26}$$

To achieve a small output fluctuation, H is desirably a constant value under different misalignments. Next, we will discuss how to achieve this goal. Since n_i is approximately the turns ratio of L_p and L_{si}, and k_i is the coupling between L_{si} and L_p, the design of H can be reduced to the design of DD2Q receiver set. As defined in (26), H is the sum of H_{DD} and $H_{Q\Sigma}$. Also, H_{DD} and $H_{Q\Sigma}$ are related to the parameters of DD-sec winding and the quadrature windings Q1 and Q2, respectively. Since the S/P-P converter with the DD-DD2Q structure at the aligned position has the same characteristics as the conventional S/P compensated converter with the DD-DD structure, the design of the DD receiver part and the variation of H_{DD} for the DD-DD2Q transformer are the same as those of the conventional DD-DD transformer. Considering the design of the DD-DD transformer has been discussed previously [29], we will focus on the design of the quadrature windings Q1 and Q2 to reduce the output fluctuation with a given DD pad.

Fig. 11 shows the structure of the DD2Q receiver, labeled with geometric parameters l_{Q1}, l_{Q2}, l_{DD}, w_{Q1}, w_{Q2}, w_{DD}, and Δw. Here, Q1 and Q2 are symmetrically wound, satisfying $l_{Q1}=l_{Q2}$ and $w_{Q1}=w_{Q2}$. Since Q1 and Q2 have no improvement in the longitudinal misalignment, only lateral and angular misalignments need to be considered here.

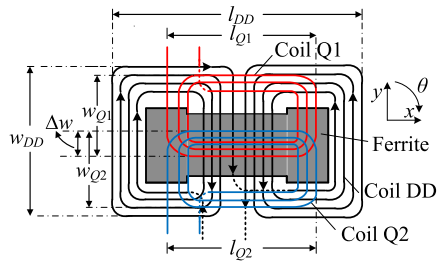

Fig. 11. Structure of DD2Q receiver set.

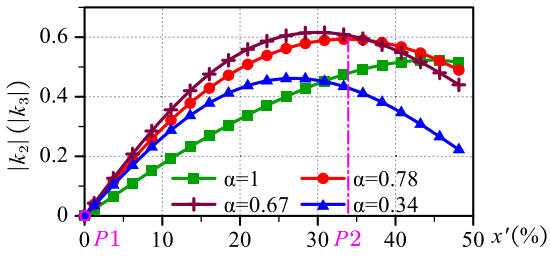

Fig. 13. Simulated k_2 and k_3 under lateral misalignment.

TABLE VII
PARAMETERS OF PRI-DD AND SEC-DD

N_p:N_{s1}	Gap /cm	l_{DD}/cm	w_{DD}/cm	L_p/μH	L_{s1}/μH	k_{1_0}	r_p/Ω	r_{s1}/Ω
12:12	2 cm	14.5	8.5	24.95	25.26	0.47	0.165	0.18

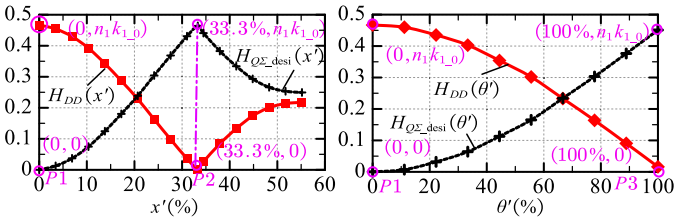

Fig. 12. H_{DD} and $H_{Q\Sigma\_\mathrm{desi}}$ under (a) lateral and (b) angular misalignment.

A. Plotting the Curve of H_{DD} and Obtaining $H_{Q\Sigma\_\mathrm{desi}}$

The same DD-DD transformer as published in [32] is used for illustration. The parameters are given in Table VII, where N_p and N_{si} are the coil turns of L_p and L_{si}, respectively. Also, $N_p = N_{s1}$ gives $n_1 \approx 1$. Equation (25) indicates that the coupling k_{1_0} and the turns ratio of N_p to N_{s1} determine the output voltage gain of the S/P-P converter operating at ω_s and the aligned position. This is one of the design considerations for N_p and N_{s1}. Combined with the measured k_1, the curves of H_{DD} versus the normalized $\triangle x$, denoted by x'(%), and the normalized $\triangle\theta$, denoted by θ'(%), can be plotted, as shown in Fig. 12. Moreover, x'(%), y'(%), and θ'(%) equal to $\Delta x/l_{\mathrm{DD}} \times 100\%$, $\Delta y/w_{\mathrm{DD}} \times 100\%$, and $\Delta\theta/90^\circ \times 100\%$, respectively. At some specific points, namely P1 ($x = 0$), P2 ($x = 1/3l_{\mathrm{DD}}$), and P3 ($\theta = 90^\circ$), the conditions $H_{\mathrm{DD}}|_{P1} = n_1k_{1\_0}$, $H_{DD}|_{P2} = 0$ [23] and $H_{DD}|_{P3} = 0$ always hold for the symmetrical structure for the two DD coils. To achieve a constant H, the desired $H_{Q\sum\_\mathrm{desi}}$ should satisfy

$$H_{Q\Sigma\_\mathrm{desi}} + H_{\mathrm{DD}} = H = H_{Q\Sigma\_\mathrm{desi}}|_{P1} + H_{\mathrm{DD}}|_{P1} = n_1k_{1\_0}. \tag{27}$$

Then, the curves of $H_{Q\Sigma\_\mathrm{desi}}$ can be plotted, as shown by the black dashed line in Fig. 12. Obviously

$$H_{Q\Sigma\_\mathrm{desi}}|_{P1} = 0,\ H_{Q\Sigma\_\mathrm{desi}}|_{P2} = H_{Q\Sigma\_\mathrm{desi}}|_{P3} = n_1k_{1\_0}. \tag{28}$$

B. Determining the Geometric Dimensions

To achieve a nearly constant H, the actual $H_{Q\sum}$ should be as close to $H_{Q\sum\_\mathrm{desi}}$ as possible. As shown in (26), $H_{Q\sum} \approx 2|k_2n_2/(1+k_{e2})|$. We will discuss the effect of geometric parameters of Q1 and Q2 on the coupling coefficients, and then provide a design method for selecting the parameters.

1) Coil Length l_{Q1}, l_{Q2}: To normalize the coil lengths l_{Q1} and l_{Q2} by l_{DD}, define $\alpha = l_{Q1}/l_{\mathrm{DD}} = l_{Q2}/l_{\mathrm{DD}}$. By simulation with Ansoft 2-D, the curves of k_2 versus x'(%) for different values of α are obtained, as shown in Fig. 13. It can be seen that the position of the maximum k_2 changes with α, and it happens around P2 when α ranges from 0.67 to 0.78. We choose l_{Q1} and l_{Q2} as $0.78l_{DD}$ for maximum k_2 that occurs at P2.

2) Overlap Distance Δw: The overlap distance Δw between Q1 and Q2 affects the mutual inductance M_c, and hence affects the values of L_{ei} and k_{ei}. From Figs. 8 and 10, and (14), it can be derived that $L_{ei} = M_c$ under lateral misalignment and $L_{ei} = -M_c$ under angular misalignment. If k_{ei} is nonzero, the designed values of C_{si} are different for the two cases, affecting the output characteristics. Therefore, in this case, M_c is nullified by adjusting the overlap distance Δw, which can be determined by using the analytical model proposed in [28].

3) Coil Width w_{Q1}, w_{Q2}: Fig. 12 indicates that there is the maximum value occurs at P2 or P3 for $H_{Q\sum\_\mathrm{desi}}$, and hence for $H_{Q\sum}$. Also, $H_{Q\sum}$ is proportional to k_2 according to (26), since $n_i = \sqrt{L_p/L_{si}}$ and $k_{e2} = L_{e2}/\sqrt{L_{s2}L_{s3}}$ are approximately constant under various misalignments. So, the maximum value also occurs at P2 or P3 for k_2. We use $k_{2\max\_x}$ and $k_{2\max\_\theta}$ to represent the value of k_2 at P2 and P3, respectively. The detailed values of $k_{2\max\_x}$ and $k_{2\max\_\theta}$ are determined by the coil width. Combining (26) with (28) gives

$$2n_2k_{2\max\_\theta} = 2n_2k_{2\max\_x} = n_1k_{1\_0}(1+k_{e2}). \tag{29}$$

Equation (29) gives $k_{2\max\_\theta} = k_{2\max\_x}$. By setting $\alpha = 0.78$, the simulated curves of $k_{2\max\_\theta}$ and $k_{2\max\_x}$ versus β, which is defined as $\beta = w_{Q1}/w_{\mathrm{DD}} = w_{Q2}/w_{\mathrm{DD}}$, are plotted in Fig. 14. Note that for different values of β, Δw is always adjusted to keep $M_c \approx 0$. It can be found that there are three intersection points for $k_{2\max\_\theta}$ and $k_{2\max\_x}$ for different coupling values, as marked in Fig. 14. From the aforementioned analysis, it can be found that the higher the coupling, the larger the output power. Thus, in this case, we choose $\beta = 0.61$ to achieve maximum $k_{2\max}$, yielding $w_{Q1} = w_{Q2} = 0.61w_{\mathrm{DD}}$.

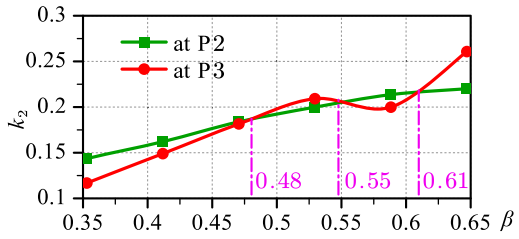

Fig. 14. Simulated k_2 at P2 and P3 versus β.

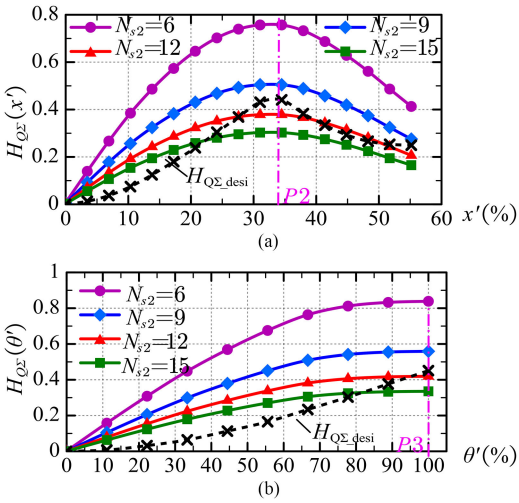

Fig. 15. $H_{Q\Sigma}$ for different N_{s2} under (a) lateral and (b) angular misalignments.

C. Determining N_{s2} and N_{s3}

The value of n_i is determined by the turns ratio of N_p and N_{si}. Since the geometric dimensions of Q1 and Q2 have been determined, the effects of N_{s2} or N_{s3} on $H_{Q\sum}$ could be investigated with the help of the simulation software Ansoft 3-D. The simulated curves of $H_{Q\sum}$ for different N_{s2} versus $x'(\%)$ and $\theta'(\%)$ are plotted in Fig. 15, where the curve of $H_{Q\Sigma\_desi}$ is also illustrated for comparison. To reduce variation of H, the actual curve of $H_{Q\sum}$ should be as close as possible to that of $H_{Q\sum\_desi}$. There are many ways to evaluate the error between $H_{Q\sum}$ and $H_{Q\sum\_desi}$. We evaluate the error according to the deviation between $H_{Q\sum}$ and $H_{Q\sum}$ at P2 and P3. We define

$$\varepsilon = (\Delta H_{Q\Sigma}|_{P2})^2 + (\Delta H_{Q\Sigma}|_{P3})^2 \tag{30}$$

where $\Delta H_{Q\sum} = |H_{Q\sum} - H_{Q\sum\_desi}|$. Obviously, the value of $H_{Q\sum}$ for $N_{s2} = 12$ gives minimum $\Delta H_{Q\sum}|_{P2}$, $\Delta H_{Q\sum}|_{P3}$, and ε among the four simulated curves. So, we choose N_{s2} and N_{s3} as 12.

D. Design Results

The design and measured parameters of Q1 and Q2 are given in Table VIII. A photo of the fabricated transformer is shown in Fig. 16. The measured coupling coefficients k_1, k_2, and k_3 under different misalignments are illustrated in Fig. 17.

TABLE VIII
DESIGN PARAMETERS OF Q1 AND Q2

N_{s2}:N_{s3}	l_{Q1} (cm)	l_{Q2} (cm)	w_{Q1} (cm)	w_{Q2} (cm)	Δw (cm)	L_{s2} (μH)	L_{s3} (μH)	r_{s2} (Ω)	r_{s3} (Ω)
12:12	11.31	11.31	5.1	5.1	2	33.25	31.1	0.20	0.21

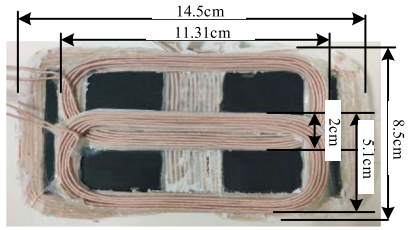

Fig. 16. Photo of the DD2Q receiver set.

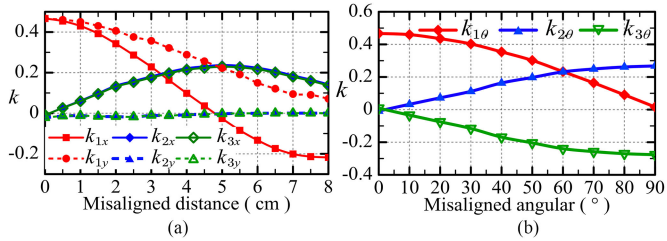

Fig. 17. Measured coupling coefficients of k_1, k_2 and k_3 (a) under lateral and longitudinal misalignment and (b) under angular misalignment.

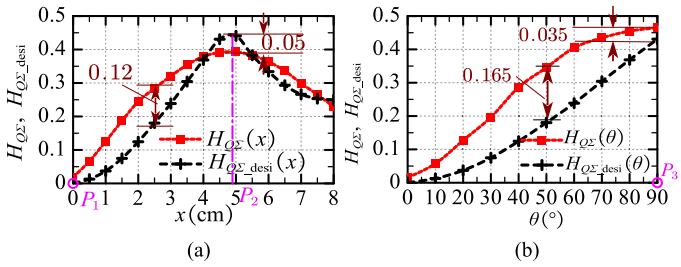

Fig. 18. $H_{Q\Sigma\_desi}$ and $H_{Q\Sigma}$ for the fabricated transformer versus (a) lateral misalignment and (b) angular misalignment.

It should be noted that distance x ranging from 0 to 8 cm corresponds to $x'(\%)$ ranging from 0% to 55%. Distance y ranging from 0 to 8 cm corresponds to $y'(\%)$ ranging from 0% to 94%. Also, angle θ ranging from 0 to 90° corresponds to $\theta'(\%)$ ranging from 0% to 100%. It can be seen that k_2 and k_3 coincide in Fig. 17(a) and they are symmetrical in Fig. 17(b), agreeing with the assumption of $|k_2| \approx |k_3|$ in previous analysis.

The actual $H_{Q\Sigma}$ for the DD-DD2Q transformer is plotted in Fig. 18 along with the desired $H_{Q\sum\_desi}$. It can be seen that $H_{Q\Sigma}$ has a small fluctuation under misalignments: $\Delta H_{Q\sum}|_{P2} = 0.05$, $\Delta H_{Q\sum}|_{P3} = 0.035$, and $\varepsilon \approx 0.004$. The maximum $\Delta H_{Q\sum}$ in lateral and angular directions are 0.12 and 0.165, respectively. According to (24) and (26), H and K can be calculated and plotted in Fig. 19. The value of ΔH in both lateral and angular directions is about 0.17. Also, K has a relatively small value that helps to obtain a load-insensitive output voltage.

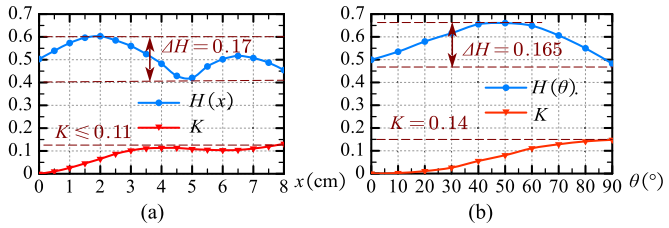

Fig. 19. H and K versus (a) lateral misalignment and (b) angular misalignment.

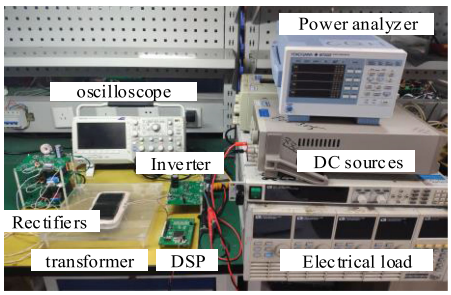

Fig. 20. Photo of the S/P-P converter.

TABLE IX
COMPONENTS OF THE PROTOTYPE

Components	Type and value
MOSFETs	BSC098N10NS5
Capacitors	C_p = 94 nF, C_{s1} = 79.53 nF, C_{s2} = 51.7 nF,C_{s3} = 56.6 nF
Filter inductors	L_{f1} = 142 μH, L_{f2} = 125 μH, L_{f3} = 125 μH
Filter capacitor	C_f = 680 μF

It should be noted that the proposed design method for the introduced Q-coil is also suitable for the DDQ receiver set.

V. EXPERIMENTAL RESULTS

A. Parameters of S/P-P Converter

A prototype of the S/P-P converter adopting the DD-DD2Q transformer, as shown in Fig. 16, is built to verify the analysis. The input dc voltage is 30 V and the rated output power is 100 W. The photo of the prototype is given in Fig. 20. The operating frequency is fixed at 125 kHz, which is a little higher than the secondary tuned frequency 120 kHz to achieve the ZVS for the primary switches. The detailed parameters of the resonant components are given in Table IX.

B. Operating Modes Under Misalignments

Substituting the detailed parameters into (19) and (20), we get the boundaries for the three modes under different load conditions, as shown in Fig. 21. It can be seen that the S/P-P converter allows a wide operating region for Mode 7, in which three secondary coils powering the load simultaneously, agreeing with the analysis in Section II. Besides, the region of Mode 7 for $R_L = 20\,\Omega$ is wider than that of $R_L = 40\,\Omega$.

To verify the analysis, three points in different modes are selected for test: TP2 (0 cm, 0 cm, 30°) for Mode7, TP3 (0 cm, 0 cm, 90°) for Mode 6, and TP1 (0 cm, 0 cm, 10°), for Mode 7 when $R_L = 20\,\Omega$ and for Mode 1 when $R_L = 40\,\Omega$, where (x cm, y cm, θ°) gives the respective misalignments in the x-, y- and θ- directions. The measured coefficients k_2 and k_3 at TP1, TP2, and TP3 are labeled with green and blue triangles, respectively, as shown in Fig. 21. Fig. 22 illustrates the waveforms of u_{si} and i_{Di} of the S/P-P converter at the three test points with different loads. It can be seen that, when $R_L = 20\,\Omega$, the converter operates in Mode 7 for TP1 since $|\dot{I}_{Di}| > 0$, Mode 7 for TP2 since $|\dot{I}_{Di}| > 0$ and Mode 6 for TP3 since $|\dot{I}_{D1}| = 0$. When $R_L = 40\,\Omega$, the converter operates in Mode 1 for TP1 since $|\dot{I}_{D2}| = |\dot{I}_{D3}| = 0$, Mode 7 for TP3 since $|\dot{I}_{Di}| > 0$, and Mode 6 for TP4 since $|\dot{I}_{D1}| = 0$, agreeing well with the theoretical results.

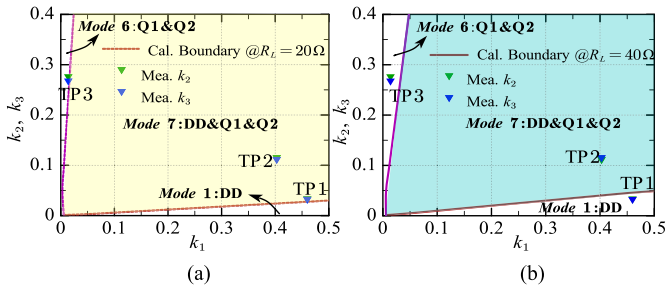

Fig. 21. Calculated operation modes on the k_1-k_2 (k_3) plane. (a) $R_L = 20\,\Omega$. (b) $R_L = 40\,\Omega$.

C. Input Waveforms and Output Voltage Gain

Fig. 23 shows the waveforms of u_{AB} and i_p under different misalignments. It can be seen that i_p is always lagging behind u_{AB} with a small phase angle, which indicates that the input impedance of S/P-P converter is weakly inductive.

According to (23), the normalized output voltage gain G_{vN}, where $G_{vN} = G_v/G_{v\_ali}$ and G_{v_ali} represents the output voltage gain at aligned position, can be approximately calculated, as shown in Fig. 24. The output voltage fluctuation δ_v, which compares the variation of outputs under different misalignments, is defined as

$$\delta_v = \frac{\Delta G_v}{G_{v\_ali}} \times 100\% = \frac{G_{v\max} - G_{v\min}}{G_{v\_ali}} \times 100\%. \quad (31)$$

It can be seen from Fig. 24 that the calculated results of δ_v according to (23) are 33% and 28% for lateral and angular misalignments, respectively.

The measured output voltage results of the S/P-P converter are shown in Fig. 25. Comparing Fig. 24 with Fig. 25, it can be seen that the measured curves have the same shape with the calculated ones using (23), and the calculated values of output fluctuation using (23) approximate to the measured values, verifying the effectiveness of the approximate analysis given in Section III-C. We also use the numerical calculation method given in Section III-B to obtain the accurate calculated results, which have been included in Fig. 25. The calculated and measured results match very well. With a maximum fluctuation of 35.6% for δ_v (corresponds to $\triangle G_v = 0.57$), the S/P-P converter

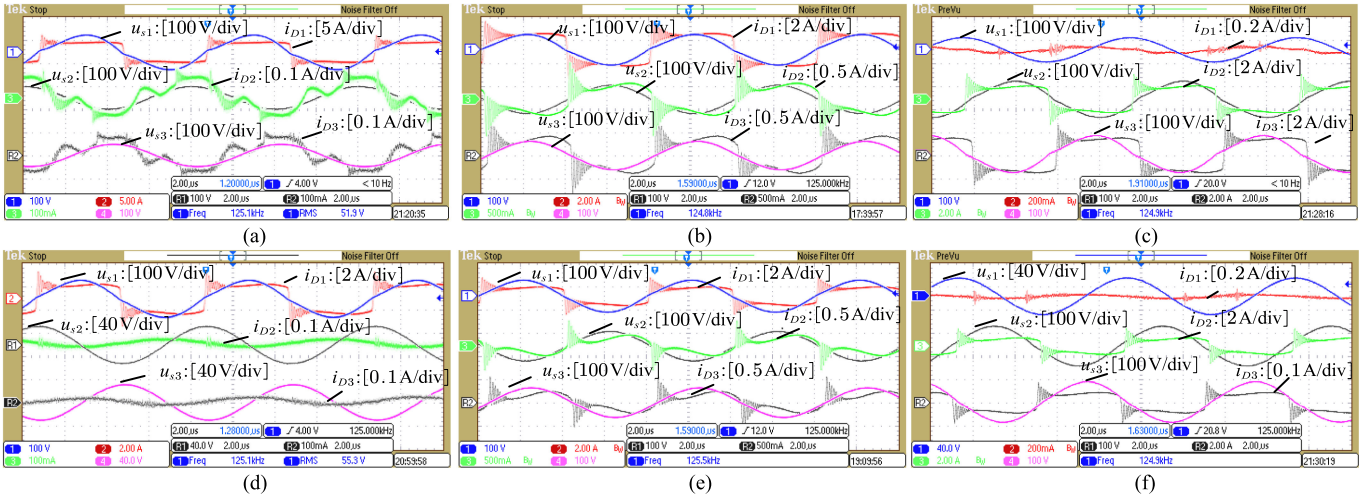

Fig. 22. Rectifier bridge input waveforms of S/P-P converter with $R_L = 20\,\Omega$ at (a) TP1, (b) TP2, and (c) TP3; with $R_L = 40\,\Omega$, at (d) TP1, (e) TP2, and (f) TP3.

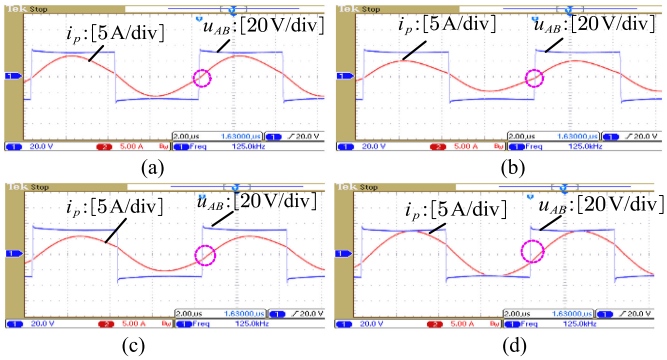

Fig. 23. Input voltage and current waveforms of S/P-P converter under different misaligned conditions with $R_L = 20\,\Omega$. (a) (0 cm, 0 cm, 0°). (b) (7 cm, 0 cm, 0°). (c) (0 cm, 3 cm, 0°). (d) (0 cm, 0 cm, 90°).

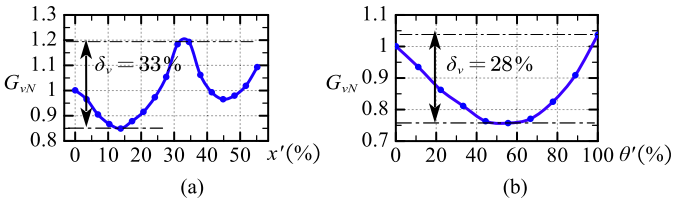

Fig. 24. Calculated voltage gain according to (23) under (a) lateral misalignment and (b) angular misalignment.

with the optimized DD2Q receiver, allows approximately 55% lateral misalignment, 44% longitudinal misalignment and 100% angular misalignment, as shown in Fig. 25.

Adopting S/P compensation, converters using DD and DDQ receiver sets, are also tested for comparison. The dimensions for the DD coil of the receiver pads are the same as those of the DD2Q. The quadrature winding Q in DDQ is also optimized to achieve a nearly constant H under lateral misalignment. Experiments are conducted sharing the primary parts of the S/P-P converter. The measured results are given in Fig. 26.

TABLE X
MISALIGNMENT TOLERANCE FOR THREE RECEIVER PADS

Secondary coil	DD	DDQ	DD2Q
$x'(\%)$	16%	55%	55%
$y'(\%)$	43%	46%	44%
$\theta'(\%)$	49%	51%	100%

Obviously, null points exist in the voltage gain curves for both DD and DDQ receivers; however, the DD2Q receiver has no null values, ensuring good system performance. The converters exhibit similar performance of the output voltage with the DDQ and DD2Q receivers under lateral and longitudinal misalignment. For brevity, the voltage gain curves are omitted (refer to [32]). With the a maximum fluctuation of 35.6% for δ_v, the misalignment tolerance for the three receivers can be obtained, as listed in Table X. Compared with the DD receiver, the lateral and angular misalignment tolerances of the proposed DD2Q coil sets increase by about 39% and 51%, respectively.

Furthermore, the output voltage of the S/P-P converter are tested when considering the combination of x-, y- and θ- misalignments with $R_L = 20\,\Omega$. Fig. 27(a) shows the measured voltage gain G_v, as well as the fitting surface, versus different combinations of $x'(\%)$ and $y'(\%)$ when $\theta' = 0$. The value of δ_v is 29.03% within the region of $x' \leq 55\%$ and $y' \leq 50\%$. Fig. 27(b) shows the voltage gain under different combinations of $x'(\%)$, $y'(\%)$, and $\theta'(\%)$, when letting $x'(\%) = y'(\%)$. Obviously, δ_v is 43.87%. Thus, with the limitation of 50% for δ_v, the maximum allowable diagonal misalignment, which is defined as $x' = y'$, is up to 50% with 100% angular misalignment.

D. Efficiency

The dc–dc efficiencies of the proposed S/P-P converter are measured and shown in Fig. 28, where the results of the converter using the DD receiver are also included for comparison. Obviously, the efficiency of the DD2Q receiver is significantly

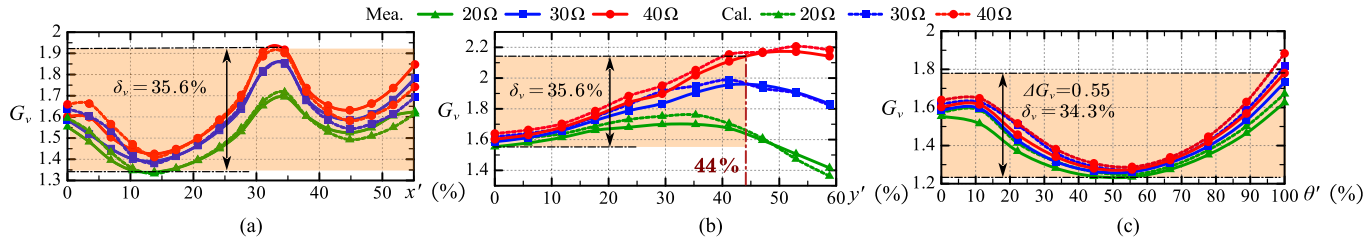

Fig. 25. Voltage gain of S/P-P converter with DD2Q structure under (a) lateral, (b) longitudinal, and (c) angular misalignments.

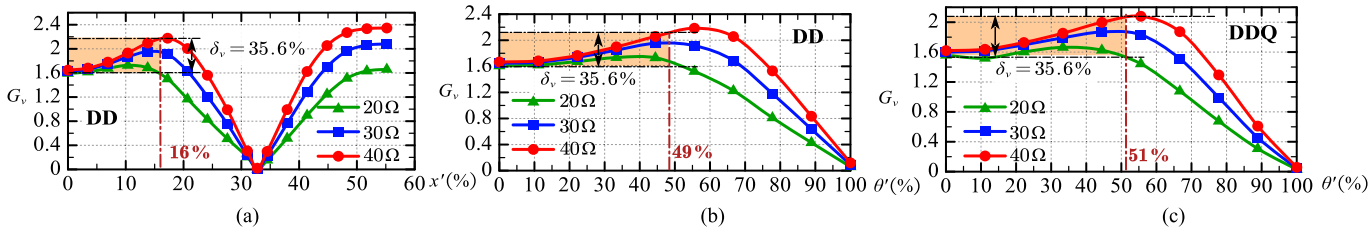

Fig. 26. Voltage gain for DD or DDQ receiver pad. (a) DD, lateral misalignment. (b) DD, angular misalignment. (c) DDQ, angular misalignment. *Note: x'(%), y'(%),* and *θ'(%)* equal to $\Delta x/l_{\mathrm{DD}} \times 100\%$, $\Delta y/w_{\mathrm{DD}} \times 100\%$, and $\Delta\theta/90^\circ \times 100\%$, respectively.

TABLE XI
PERFORMANCE COMPARISONS

		Cost	Coupling range [/ relative misalignment]	Output fluctuation	Efficiency range	Having the null coupling problem?	Output variation against load
S/P-P converter in *x* axis		High	-0.18 to 0.47[(1)], [55%]	35.6%	88.8% to 92.27%	No	Small
Compensation	S/P [19]	Low	[30%]	38%	80.2% to 90.5%	Yes	Large
	PS/S [17]	Medium	0.21-0.55	48.3%	84.68%	Yes	Small
	SP/S [18]	Medium	[25%]	/[(2)]	/[(2)]	Yes	Large
	LCC/S [21]	Medium	0.18-0.32	20%	88.5%-93%	Yes	Medium

Note: [(1)] The negative sign "-" indicates negative coupling; [(2)] "/" means that the detailed data is not given in the literature.

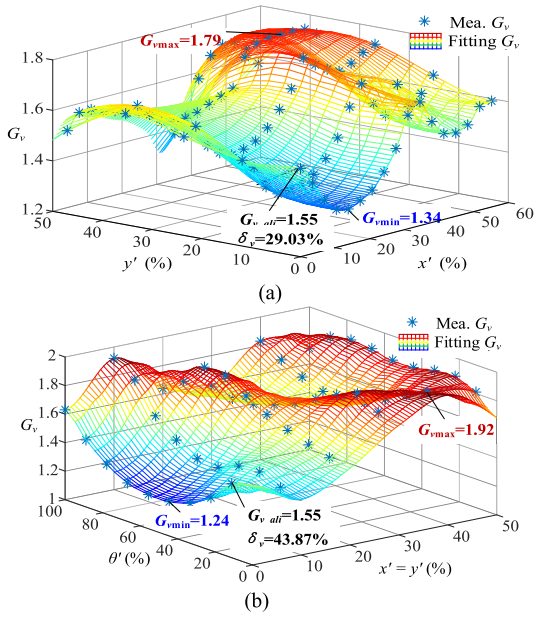

Fig. 27. Voltage gain measured under horizontal misalignments of S/P-P converter ($R_L = 20\,\Omega$). (a) $\theta' = 0$. (b) $x' = y'$.

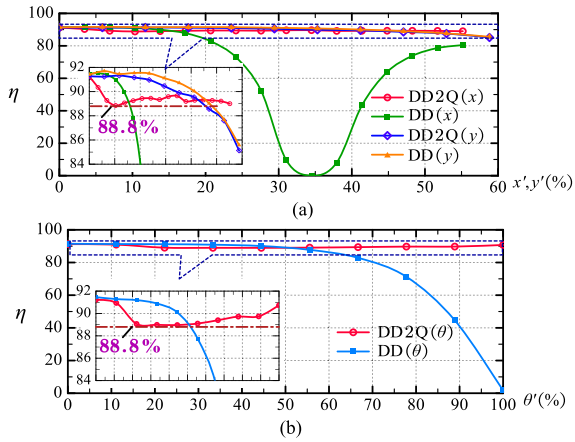

Fig. 28. Efficiency for DD and DD2Q receiver under (a) lateral or longitudinal misalignment and (b) angular misalignment. ($R_L = 30\,\Omega$.).

improved under larger lateral and angular misalignments. When under small misaligned distance, the efficiency of DD2Q receiver is slightly lower due to the circulating currents in the quadrature windings.

TABLE XII
OUTPUT VOLTAGE GAIN AND INPUT IMPEDANCE

Modes	Output to input voltage gain G_v	Input impedance Z_{in}
Mode 1	$G_v = \frac{8}{\pi^2}\left\lvert\frac{j\omega M_1}{Z_{in}(j\omega L_{s1}G_E+1-\omega^2/\omega_s^2)}\right\rvert = \frac{8}{\pi^2}L_{s1}\big/M_1\big\rvert_{\omega=\omega_s}$	$Z_{in} = Z_p + \frac{(\omega M_1)^2}{j\omega L_{s1}+\frac{1}{j\omega C_{s1}+G_E}} + \sum_{i=2}^{3}\frac{(\omega M_i)^2}{j\omega L_{si}+j\omega L_{ei}+\frac{1}{j\omega C_{si}}} \approx \left(\frac{M_1}{L_{s1}}\right)^2\frac{1}{G_E}\big\rvert_{\omega=\omega_s}$
Mode 7	$G_v = \frac{8}{\pi^2}\left\lvert\frac{j\omega M_1}{Z_{in}(j\omega L_{s1}G_{E1}+1-\omega^2/\omega_s^2)}\right\rvert = \frac{8}{\pi^2}\left\lvert\frac{\left\lvert\frac{M_1}{L_{s1}}\right\rvert+\left\lvert\frac{M_2}{L_{s2}+L_{e2}}\right\rvert+\left\lvert\frac{M_3}{L_{s3}+L_{e3}}\right\rvert}{Z_{in}\rvert_{\omega=\omega_s}G_E}\right\rvert_{\omega=\omega_s}$	$Z_{in} = Z_p + \frac{(\omega M_1)^2}{j\omega L_{s1}+\frac{1}{j\omega C_{s1}+G_{E1}}} + \sum_{i=2}^{3}\frac{(\omega M_i)^2}{j\omega L_{si}+j\omega L_{ei}+\frac{1}{j\omega C_{si}+G_{Ei}}} \approx j\omega_s L_p\left[k_{1\_0}^2-\left(k_1^2+\frac{k_2^2}{1+k_{e2}}+\frac{k_3^2}{1+k_{e3}}\right)\right]+\frac{1}{G_E}\left(\frac{\lvert M_1\rvert}{L_{s1}}+\sum_{i=2}^{3}\frac{\lvert M_i\rvert}{L_{si}+L_{ei}}\right)^2\Big\rvert_{\omega=\omega_s}$
Mode 6	$G_v = \frac{8}{\pi^2}\left\lvert\frac{j\omega M_2}{Z_{in}(j\omega L_{s2}G_{E2}+1-\omega^2/\omega_s^2)}\right\rvert = \frac{8}{\pi^2}\left\lvert\frac{\left\lvert\frac{M_2}{L_{s2}+L_{e2}}\right\rvert+\left\lvert\frac{M_3}{L_{s3}+L_{e3}}\right\rvert}{Z_{in}\rvert_{\omega=\omega_s}G_E}\right\rvert_{\omega=\omega_s}$	$Z_{in} = Z_p + \frac{(\omega M_1)^2}{j\omega L_{s1}+\frac{1}{j\omega C_{s1}+G_{E1}}} + \sum_{i=2}^{3}\frac{(\omega M_i)^2}{j\omega L_{si}+j\omega L_{ei}+\frac{1}{j\omega C_{si}+G_{Ei}}} \approx j\omega_s L_p\left[k_{1\_0}^2-\left(\frac{k_2^2}{1+k_{e2}}+\frac{k_3^2}{1+k_{e3}}\right)\right]+\frac{1}{G_E}\left(\sum_{i=2}^{3}\frac{\lvert M_i\rvert}{L_{si}+L_{ei}}\right)^2\Big\rvert_{\omega=\omega_s}$

E. Comprehensive Performance Comparisons

A comprehensive performance comparison, including cost, coupling range, output fluctuation, efficiency, etc., between the proposed S/P-P converter and the existing compensation networks is given in Table XI. It is shown that the proposed solution alleviates the null coupling problem with improved misalignment tolerance and relatively high efficiency, at the expense of the increased usage of copper and power devices.

VI. CONCLUSION

In this article, a comprehensive investigation into the use of multicoil receiver set to improve the misalignment tolerance has been presented. After a general analysis of the operating modes and collaboration of multiple receiving coils, an S/P-P converter with a DD2Q receiver has been adopted to give a quantitative analysis of the respective operating characteristics in detail, demonstrating that the proposed S/P-P converter can effectively reduce the output fluctuation under coil misalignment. A design method for the multicoil receiver is also provided. Prototypes of resonant converters using DD2Q secondary, DD secondary, and optimized DDQ secondary are fabricated for verification and comparison. The experimental results match well with the analytical results, verifying that the designed DD2Q structure can maintain a stable output voltage over high misalignment in the x-, y- and θ- directions. The proposed analysis method of the converter and design method of the receiver can also be applied to other multicoil receiver structures and other connections. The proposed approach is suitable for charging applications in low-power planar wireless charging pad systems and high-power electric vehicles, such as modern trams, automatic guided vehicles, and passenger cars.

APPENDIX

Using the terms of L_{e2} and L_{e3}, (12) can be represented as

$$\begin{bmatrix}\dot{U}_{AB}\\0\\0\\0\end{bmatrix} = \begin{bmatrix} Z_p & -j\omega M_1 & -j\omega M_2 & -j\omega M_3 \\ -j\omega M_1 & Z_{s1} & 0 & 0 \\ -j\omega M_2 & 0 & Z_{s2}+j\omega L_{e2} & 0 \\ -j\omega M_3 & 0 & 0 & Z_{s3}+j\omega L_{e3}\end{bmatrix} \times \begin{bmatrix}\dot{I}_p\\ \dot{I}_{s1}\\ \dot{I}_{s2}\\ \dot{I}_{s3}\end{bmatrix}. \tag{A1}$$

Since $|\dot{U}_{si}| = |\dot{I}_{si}|/(j\omega C_{si}+G_{Ei})$, we have

$$\begin{cases}\left|\dot{U}_{s1}\right| = \left|\dfrac{\dot{U}_{AB}j\omega M_1}{Z_{\text{in}}\left(j\omega L_{s1}G_{E1}+1-\omega^2 L_{s1}C_{s1}\right)}\right| \\ \left|\dot{U}_{s2}\right| = \left|\dfrac{\dot{U}_{AB}j\omega M_2}{Z_{\text{in}}\left[j\omega(L_{s2}+L_{e2})\,G_{E2}+1-\omega^2(L_{s2}+L_{e2})\,C_{s2}\right]}\right| \\ \left|\dot{U}_{s3}\right| = \left|\dfrac{\dot{U}_{AB}j\omega M_3}{Z_{\text{in}}\left[j\omega\,(L_{s3}+L_{e3})\,G_{E3}+1-\omega^2\,(L_{s3}+L_{e3})\,C_{s3}\right]}\right|\end{cases} \tag{A2}$$

and

$$Z_{\text{in}} = Z_p + \frac{(\omega M_1)^2}{j\omega L_{s1}+\frac{1}{j\omega C_{s1}+G_{E1}}} + \sum_{i=2}^{3}\frac{(\omega M_i)^2}{j\omega L_{si}+j\omega L_{ei}+\frac{1}{j\omega C_{si}+G_{Ei}}}. \tag{A3}$$

According to the analysis of the operating modes in Section II-B, it can be found that for Mode 1

$$\left|\dot{U}_{s1}\right| = \frac{\pi U_O}{2\sqrt{2}}, \left|\dot{I}_{D1}\right| > 0 \text{ and } \left|\dot{I}_{D2}\right| = \left|\dot{I}_{D3}\right| = 0. \quad \text{(A4)}$$

For Mode 6, we have

$$\left|\dot{U}_{s2}\right| = \left|\dot{U}_{s3}\right| = \frac{\pi U_O}{2\sqrt{2}}, \left|\dot{I}_{D2}\right| > 0, \left|\dot{I}_{D3}\right| > 0 \text{ and } \left|\dot{I}_{D1}\right| = 0. \quad \text{(A5)}$$

For Mode 7, we have

$$\left|\dot{U}_{s1}\right| = \left|\dot{U}_{s2}\right| = \left|\dot{U}_{s3}\right| = \frac{\pi U_O}{2\sqrt{2}}, \left|\dot{I}_{D2}\right| > 0, \left|\dot{I}_{D3}\right| > 0 \text{ and } \left|\dot{I}_{D1}\right| > 0. \quad \text{(A6)}$$

Using Table IV, (18), and combining (A2) and (A3) yield the dc voltage gain, which has been defined in (17), and the input impedance for Mode 1, Mode 6, and Mode 7, as listed in Table XII.

The boundary between Modes 1 and 7 is determined by the conditions

$$\left|\dot{U}_{s1}\right| = \sqrt{2}\left|\dot{U}_{s2}\right| = \sqrt{2}\left|\dot{U}_{s3}\right|, G_{E2} = G_{E3} = 0. \quad \text{(A7)}$$

And the boundary between Modes 6 and 7 is determined by the conditions

$$\sqrt{2}\left|\dot{U}_{s1}\right| = \left|\dot{U}_{s2}\right| = \left|\dot{U}_{s3}\right|, G_{E1} = 0. \quad \text{(A8)}$$

Combining the corresponding formulas in Table IV, with (16), (18), (A7), and (A8), the boundary between Mode 1 and Mode 7, and that between Mode 7 and Mode 6 can be derived as shown in (19) and (20).

REFERENCES

[1] G. A. Covic and J. T. Boys, "Inductive power transfer," *Proc. IEEE*, vol. 101, no. 6, pp. 1276–1289, Jun. 2013.

[2] Z. Cheng, Y. Lei, K. Song, and C. Zhu, "Design and loss analysis of loosely coupled transformer for an underwater high-power inductive power transfer system," *IEEE Trans. Magn.*, vol. 51, no. 7, pp. 1–10, Jul. 2015.

[3] J. S. Ho, S. Kim, and A. S. Y. Poon, "Midfield wireless powering for implantable systems," *Proc. IEEE*, vol. 101, no. 6, pp. 1369–1378, Jun. 2013.

[4] M. Lu, M. Bagheri, A. P. James, and T. Phung, "Wireless charging techniques for UAVS: A review, reconceptualization, and extension," *IEEE Access*, vol. 6, pp. 29865–29884, 2018.

[5] S. Li and C. C. Mi, "Wireless power transfer for electric vehicle applications," *IEEE J. Emerg. Sel. Top. Power Electron.*, vol. 3, no. 1, pp. 4–17, Mar. 2015.

[6] K. Fotopoulou and B. W. Flynn, "Wireless power transfer in loosely coupled links: Coil misalignment model," *IEEE Trans. Magn.*, vol. 47, no. 2, pp. 416–430, Feb. 2011.

[7] C. Y. Huang, G. A. Covic, and J. T. Boys, "Resonant network design considerations for variable coupling lumped coil systems," in *Proc. IEEE Energy Convers. Congr. Expo.*, 2012, pp. 3841–3847.

[8] A. Ahmad, M. S. Alam, and R. Chabaan, "A comprehensive review of wireless charging technologies for electric vehicles," *IEEE Trans. Transp. Electrific.*, vol. 4, no. 1, pp. 38–63, Mar. 2018.

[9] D. Patil, M. K. McDonough, J. M. Miller, B. Fahimi, and P. T. Balsara, "Wireless power transfer for vehicular applications: Overview and challenges," *IEEE Trans. Transp. Electrific.*, vol. 4, no. 1, pp. 3–37, Mar. 2018.

[10] L. Xu, Q. Chen, X. Ren, S. C. Wong, and C. K. Tse, "Self-oscillating resonant converter with contactless power transfer and integrated current sensing transformer," *IEEE Trans. Power Electron.*, vol. 32, no. 6, pp. 4839–4851, Jun. 2017.

[11] Y. Lim, H. Tang, S. Lim, and J. Park, "An adaptive impedance-matching network based on a novel capacitor matrix for wireless power transfer," *IEEE Trans. Power Electron.*, vol. 29, no. 8, pp. 4403–4413, Aug. 2014.

[12] A. P. Hu and S. Hussmann, "Improved power flow control for contactless moving sensor applications," *IEEE Power Electron. Lett.*, vol. 2, no. 4, pp. 135–138, Dec. 2004.

[13] J. U. W. Hsu, A. P. Hu, and A. Swain, "A wireless power pickup based on directional tuning control of magnetic amplifier," *IEEE Trans. Ind. Electron.*, vol. 56, no. 7, pp. 2771–2781, Jul. 2009.

[14] E. Gati, G. Kampitsis, I. Stavropoulos, S. Papathanassiou, and S. Manias, "Wireless phase-locked loop control for inductive power transfer systems," in *Proc. IEEE Appl. Power Electron. Conf. Expo.*, 2015, pp. 1601–1607.

[15] J. Zhao, T. Cai, S. Duan, H. Feng, C. Chen, and X. Zhang, "A general design method of primary compensation network for dynamic WPT system maintaining stable transmission power," *IEEE Trans. Power Electron.*, vol. 31, no. 12, pp. 8343–8358, Dec. 2016.

[16] J. Hou, Q. Chen, S. C. Wong, C. K. Tse, and X. Ruan, "Analysis and control of series/series-parallel compensated resonant converter for contactless power transfer," *IEEE J. Emerg. Sel. Top. Power Electron*, vol. 3, no. 1, pp. 124–136, Mar. 2015.

[17] J. Hou, Q. Chen, Z. Zhang, S. C. Wong, and C. K. Tse, "Analysis of output current characteristics for higher order primary compensation in inductive power transfer systems," *IEEE Trans. Power Electron.*, vol. 33, no. 8, pp. 6807–6821, Aug. 2018.

[18] J. L. Villa, J. Sallan, J. F. S. Osorio, and A. Llombart, "High-misalignment tolerant compensation topology for ICPT systems," *IEEE Trans. Ind. Electron.*, vol. 59, no. 2, pp. 945–951, Feb. 2012.

[19] W. Gao, Q. Chen, Y. Geng, X. Ren, and S. C. Wong, "Equivalency analysis of primary series- and series-parallel-compensated contactless resonant converter," in *Proc. IEEE Appl. Power Electron. Conf. Expo.*, 2017, pp. 3259–3264.

[20] S. Li, W. Li, J. Deng, T. D. Nguyen, and C. C. Mi, "A double-sided LCC compensation network and its tuning method for wireless power transfer," *IEEE Trans. Veh. Technol.*, vol. 64, no. 6, pp. 2261–2273, Jun. 2015.

[21] H. Feng, T. Cai, S. Duan, J. Zhao, X. Zhang, and C. Chen, "An LCC-compensated resonant converter optimized for robust reaction to large coupling variation in dynamic wireless power transfer," *IEEE Trans. Ind. Electron.*, vol. 63, no. 10, pp. 6591–6601, Oct. 2016.

[22] S. Y. Choi, J. Huh, W. Y. Lee, and C. T. Rim, "Asymmetric coil sets for wireless stationary EV chargers with large lateral tolerance by dominant field analysis," *IEEE Trans. Power Electron.*, vol. 29, no. 12, pp. 6406–6420, Dec. 2014.

[23] G. Ke, Q. Chen, L. Xu, S. C. Wong, and C. K. Tse, "A model for coupling under coil misalignment for DD pads and circular pads of WPT system," in *Proc. IEEE Energy Convers. Congr. Expo.*, 2016, pp. 1–6.

[24] S. Kim, G. A. Covic, and J. T. Boys, "Tripolar pad for inductive power transfer systems for EV charging," *IEEE Trans. Power Electron.*, vol. 32, no. 7, pp. 5045–5057, Jul. 2017.

[25] A. Zaheer, H. Hao, G. A. Covic, and D. Kacprzak, "Investigation of multiple decoupled coil primary pad topologies in lumped IPT systems for interoperable electric vehicle charging," *IEEE Trans. Power Electron.*, vol. 30, no. 4, pp. 1937–1955, Apr. 2015.

[26] D. Lin, C. Zhang, and S. Y. R. Hui, "Mathematic analysis of omnidirectional wireless power transfer—Part-II: Three-dimensional systems," *IEEE Trans. Power Electron.*, vol. 32, no. 1, pp. 613–624, Jan. 2017.

[27] B. H. Choi, E. S. Lee, Y. H. Sohn, G. C. Jang, and C. T. Rim, "Six degrees of freedom mobile inductive power transfer by crossed dipole TX and RX coils," *IEEE Trans. Power Electron.*, vol. 31, no. 4, pp. 3252–3272, Apr. 2016.

[28] S. Y. Choi, S. Y. Jeong, E. S. Lee, B. W. Gu, S. W. Lee, and C. T. Rim, "Generalized models on self-decoupled dual pick-up coils for large lateral tolerance," *IEEE Trans. Power Electron.*, vol. 30, no. 11, pp. 6434–6445, Nov. 2015.

[29] M. Budhia, J. T. Boys, G. A. Covic, and C.-Y. Huang, "Development of a single-sided flux magnetic coupler for electric vehicle IPT charging systems," *IEEE Trans. Ind. Electron.*, vol. 60, no. 1, pp. 318–328, Jan. 2013.

[30] A. Zaheer, D. Kacprzak, and G. A. Covic, "A bipolar receiver pad in a lumped IPT system for electric vehicle charging applications," in *Proc. IEEE Energy Convers. Congr. Expo.*, 2012, pp. 283–290.

[31] "Surface vehicle information report J2954, November 2017," SAE Int., Warrendale, PA, USA, 2017.

[32] G. Ke, Q. Chen, W. Gao, S. C. Wong, and C. K. Tse, "Power converter with novel transformer structure for wireless power transfer using a DD2Q power receiver coil set," in *Proc. IEEE Energy Convers. Congr. Expo.*, 2016, pp. 1–6.

[33] J. P. W. Chow, N. Chen, H. S. H. Chung, and L. L. H. Chan, "An investigation into the use of orthogonal winding in loosely coupled link for improving power transfer efficiency under coil misalignment," *IEEE Trans. Power Electron.*, vol. 30, no. 10, pp. 5632–5649, Oct. 2015.

[34] Y. Zhang, Q. Chen, X. Ren, S.-C. Wong, Z. Zhang, and W. Hua, "Design of S/P compensated IPT system considering parameter variations in consideration of ZVS achievement," in *Proc. IEEE Energy Convers. Congr. Expo.*, 2016, pp. 1–6.

Guangjie Ke received the B.S. and M.S. degrees in electrical engineering in 2015 and 2018, respectively, from the Nanjing University of Aeronautics and Astronautics, Nanjing, China, where she is currently working toward the Ph.D. degree.

Her current research interests include contactless resonant converters and wireless power transfer system.

Qianhong Chen (M'06) received the B.S., M.S., and Ph.D. degrees in electrical engineering from the Nanjing University of Aeronautics and Astronautics (NUAA), Nanjing, China, in 1995, 1998, and 2001, respectively.

She is currently a Professor with the Department of Electrical Engineering, NUAA. She has authored/coauthored more than 70 papers in international journals and conferences. Her research interests include application of integrated-magnetics, wireless power transfer, and high power density power converters.

Wei Gao received the B.S. and M.S. degrees in electrical engineering from the Nanjing University of Aeronautics and Astronautics, Nanjing, China, in 2016 and 2019, respectively.

His research interests include inductive power transfer, dc–dc converter, and high-performance battery chargers for power bank.

Siu-Chung Wong (M'01–SM'09) received the B.Sc. degree in physics from the University of Hong Kong, Hong Kong, in 1986, the M.Phil. degree in electronics from the Chinese University of Hong Kong, Hong Kong, in 1989, and the Ph.D. degree from the University of Southampton, Southampton, U.K., in 1997.

He joined the Hong Kong Polytechnic University in 1988 as an Assistant Lecturer. He is currently an Associate Professor with the Department of Electronic and Information Engineering, Hong Kong Polytechnic University, where he conducts research in power electronics.

Dr. Wong is a member of the Electrical College, Institution of Engineers, Australia.

Chi K. Tse (M'90–SM'97–F'06) received the B.Eng. (Hons.) degree with first class honors in electrical engineering and the Ph.D. degree from the University of Melbourne, Australia, in 1987 and 1991, respectively.

He is currently a Chair Professor of Electrical Engineering with City University of Hong Kong, Hong Kong. His research interests include power electronics, nonlinear systems and complex network applications.

He was awarded a number of research and industry awards, including Prize Paper Awards by IEEE TRANSACTIONS ON POWER ELECTRONICS in 2001 and 2015, RISP Journal of Signal Processing Best Paper Award in 2014, Best Paper Award by International Journal of Circuit Theory and Applications in 2003, two Gold Medals at the International Inventions Exhibition in Geneva in 2009 and 2013, a Silver Medal at the International Invention Innovation Competition in Canada in 2016, a Grand Prize and Gold Medal at the Silicon Valley International Invention Festival in 2019, and a number of recognitions by the academic and research communities, including honorary professorship by several Chinese and Australian universities, Chang Jiang Scholar Chair Professorship, IEEE Distinguished Lecturership, Distinguished Research Fellowship by the University of Calgary, Gledden Fellowship and International Distinguished Professorship-at-Large by the University of Western Australia. While with the Hong Kong Polytechnic University, he received the President's Award for Outstanding Research Performance twice, Faculty Research Grant Achievement Award twice, Faculty Best Researcher Award, and several teaching awards. Dr. Tse serves and has served as the Editor-in-Chief for the IEEE TRANSACTIONS ON CIRCUITS AND SYSTEMS II from 2016 to 2019, *IEEE Circuits and Systems Magazine* from 2012 to 2015, IEEE CIRCUITS AND SYSTEMS SOCIETY NEWSLETTER since 2007, the Associate Editor for three IEEE Journal/Transactions, the Editor for *International Journal of Circuit Theory and Applications*, and is on the Editorial Boards of a few other journals. He currently chairs the Steering Committee for the IEEE TRANSACTIONS ON NETWORK SCIENCE AND ENGINEERING. He also serves as panel member of Hong Kong Research Grants Council, and member of several professional and government committees.

Zhiliang Zhang (S'03–M'09–SM'14) received the B.Sc. and M.Sc. degrees from the Nanjing University of Aeronautics and Astronautics (NUAA), Nanjing, China, in 2002 and 2005, respectively, and the Ph.D. degree from Queen's University, Kingston, ON, Canada, in 2009.

He is currently a Professor with the Aero-Power Sci-Tech Center, NUAA. He has authored or coauthored 45 papers in the IEEE TRANSACTIONS ON POWER ELECTRONICS, and more than 80 papers in IEEE conferences. He holds 12 China patents and one U.S. patent. He coauthored the book *High Frequency MOSFET Gate Drivers: Technologies and Applications*. His research interests include high-frequency power conversion with wide bandgap devices.

Dr. Zhang was the recipient of the National Excellent Youth Fund from the National Natural Science Foundation of China in 2017.